

UNIVERSITY OF CRETE

**DEPARTMENT OF MATERIALS SCIENCE AND
TECHNOLOGY**

&

**FOUNDATION FOR RESEARCH AND TECHNOLOGY HELLAS
- INSTITUTE OF ELECTRONIC STRUCTURE AND LASER**



3D Active Photonic Nanostructures

**Master Thesis of
Kabouraki Asimina-Eleni**

Supervisors

Maria Vamvakaki

Maria Farsari

HERAKLION, OCTOBER 2012

Abstract

We present our most recent results on the fabrication of 3D high-resolution photonic nanostructures containing Cadmium Sulfide (CdS) quantum dots (QDs), exhibiting higher order diffraction patterns and stop-gaps at visible wavelengths. These structures are fabricated using direct laser writing (DLW) and novel, organic-inorganic hybrid materials.

DLW by multi-photon polymerization is a nonlinear optical technique which allows the fabrication of 3D structures with a resolution beyond the diffraction limit. The polymerization process is initiated when the beam of an ultra-fast laser is focused into the volume of a transparent, photosensitive material. Multi-photon absorption takes place within the focal volume, where polymerization occurs. By moving the focused laser beam in a three-dimensional manner within the material, 3D structures can be fabricated.

The materials used in this work are photostructurable organic inorganic hybrid materials, prepared using the sol-gel process. This versatile technique has been exploited for the incorporation of inorganic networks into polymer matrices, using as monomers molecules that carry an inorganic part (which serves as the precursor to the inorganic network) and a polymerizable organic group (which acts as the precursor to the organic polymer). In the present work, we have included in the composite a quencher, allowing the fabrication of features well below the diffraction limit, and quantum dot precursors, enabling the *in situ* synthesis of CdS QDs.

We first prepared a composite material based on a polymerizable silicon precursor, and a cadmium-containing organic salt. Next, the inorganic siloxane network was formed by the sol-gel process, whereas, the photosensitivity that this material demonstrates, allowed its 3D laser structuring. Microstructures with spatial resolution below 100 nm and minimal shrinkage distortion were fabricated. Then, the microstructures were reacted with Na₂S, leading to the *in situ* synthesis of CdS quantum dots within the volume of the 3D structures. The X-Ray diffraction pattern of a CdS containing films showed three broad peaks attributed to the crystalline cubic structure of the nanoparticles. The UV-VIS absorption spectra showed a series of overlapping peaks, which are characteristic of poly-disperse CdS quantum dots formed within the material. Fluorescence spectroscopy was used to measure the emission attributed to the CdS nanoparticles which was found in the visible region of

the spectrum. Excellent quality photonic crystal woodpile structures with period as low as 500 nm were fabricated. For the first time in such structures, we show the existence of third order nonlinear effects as well as diffraction patterns and higher order stop-gaps at visible wavelengths.

Table of Contents

CHAPTER 1 INTRODUCTION.....	6
<i>1.1 Sol-Gel</i>	<i>8</i>
1.1.1 Hydrolysis.....	10
1.1.2 Condensation	13
1.1.3 Hybrid sol-gel materials.....	16
<i>1.2 Two Photon Polymerization</i>	<i>17</i>
1.2.1 Two photon absorption	17
1.2.2 Mechanism of Two Photon Polymerization.....	18
1.2.3 Applications of 2-Photon Polymerization	20
<i>1.3 Quantum Dots</i>	<i>22</i>
1.3.1 How Quantum Dots work	23
1.3.2 Quantum dot nonlinear optical effect.....	24
1.3.3 Quantum dot - polymer composites	29
<i>1.4 Photonic crystals</i>	<i>30</i>
CHAPTER 2 EXPERIMENTAL	32
2.1 Materials	34
2.2 Synthesis of the material	35
2.3 3D Microfabrication	38
2.3.1 The woodpile structure	39
2.4 Characterization Techniques	40
2.4.1 Scanning Electron Microscopy (SEM)	40
2.4.2 UV-Vis spectroscopy	42
2.4.3 Fluorescence Spectroscopy.....	43
2.4.4 X-ray Diffraction (XRD)	44
2.4.5 Z-Scan.....	45
2.4.6 White light diffraction	48
2.4.7 Pump-probe.....	49
CHAPTER 3 RESULTS & DISCUSSION	52
3.1 Cadmium composite material.....	54
3.1.1 UV-Vis spectroscopy	54
3.1.2 Photoluminescence spectroscopy.....	56
3.1.3 X-Ray Diffraction	57
3.1.4 Scanning Electron Microscopy & EDS	58
3.1.5 Z-Scan.....	63
3.2 3D structuring and characterization.....	65
3.2.1 High resolution 3D photonic crystals.....	65
3.2.2 White light diffraction	78
3.2.3 Pump probe	82
3.3 Conclusions.....	85
References	86

CHAPTER 1

INTRODUCTION

1.1 Sol-Gel

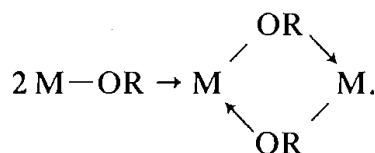
We define as *sol-gel* process the preparation of ceramic materials (or organically modified materials) by forming a sol, gelation of the sol, and the removal of the solvent. The sol is produced from inorganic or organic precursors and may consist of dense oxide particles or polymeric clusters.

The *sol-gel* process, as the name implies, involves the evolution of an inorganic network through the formation of a *sol*, and the gelation of the sol to form a network in a continuous liquid phase. A *sol* is a colloidal suspension of solid particles in a liquid. A *colloid* is a suspension in which the dispersed phase is so small (~ 1-1000 nm) that gravitational forces are negligible and interactions are dominated by short-range forces, such as van der Waals attraction and surface charges.

In the sol-gel process, the precursors for synthesizing these colloids consist of a metal or metalloid element surrounded by appropriate reactive ligands. Common precursors include inorganic salts e.g. $\text{Al}(\text{NO}_3)_3$ and hybrid compounds such as $\text{Al}(\text{OC}_4\text{H}_9)_3$. The second is a metal alkoxide, the class of precursors most widely used in sol-gel research. Metal alkoxides are members of the family of metalorganic compounds which have an organic ligand attached to a metal or metalloid atom. Commonly they are confused with organometallic compounds which are defined as having direct metal-carbon bonds, not metal-oxygen-carbon (M-O-R) linkages as in metal alkoxides. Thus metal alkoxides are not organometallic compounds, although this term is frequently used in the literature.

Transition metal alkoxides (MOR) are very popular precursors because they react readily with water. In general metal alkoxides are very reactive due to the presence of highly electronegative OR groups (hard- π donors) that stabilize the metal (M) in its highest oxidation state and render M very susceptible to nucleophilic attack. The lower electronegativity of the transition metals causes them to be more electrophilic and thus less stable towards hydrolysis, condensation and other nucleophilic reactions. Transition metals often exhibit several stable coordination numbers, and when coordinatively unsaturated, they are able to expand their coordination number via olation, oxolation, alkoxy bridging, or other nucleophilic association mechanisms. Olation is a condensation process in which a hydroxy bridge ("ol" bridge) is formed between two metal centers. Oxolation is a condensation reaction in which an oxo

bridge (-O-) is formed between two metal centers. When metal alkoxides are dissolved in non polar solvents, they form oligomers via alkoxy bridging, a nucleophilic addition (A_N) mechanism similar to olation :



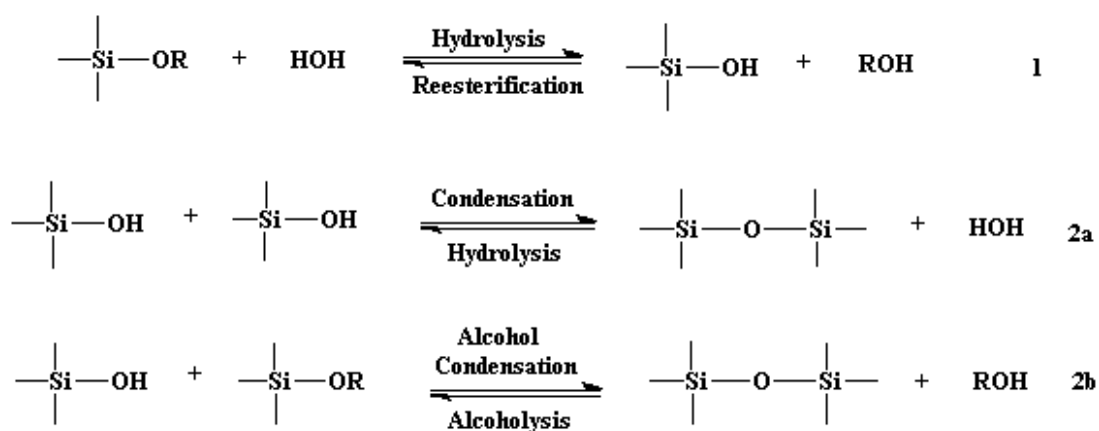
The generally rapid kinetics of nucleophilic reactions has attracted fundamental studies of the hydrolysis and condensation of transition metal alkoxides.

Generally the sol-gel process involves two main reactions:

1. Hydrolysis and
2. Condensation

However, the characteristics and properties of a particular sol-gel inorganic network are related to a number of factors that affect the rate of hydrolysis and condensation reactions, such as, pH, temperature and time of reaction, reagent concentrations, catalyst nature and concentration, aging temperature and time, and the drying process. Of the factors listed above, pH, the nature and concentration of the catalyst and the temperature have been identified as the most important.

The general reaction scheme can be seen in the following figure[1]:



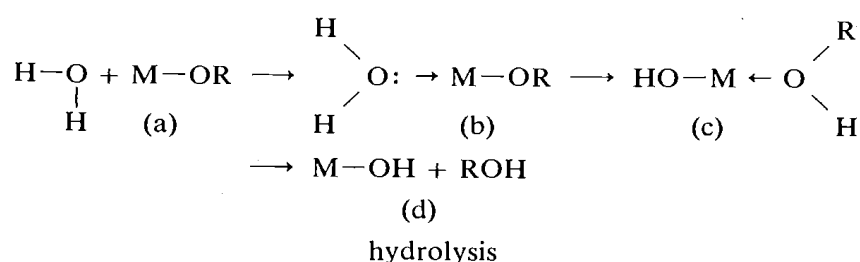
1.1.1 Hydrolysis

The reaction is called hydrolysis, because a hydroxyl ion becomes attached to the metal atom as in the following reaction:



where R represents an alkyl group and ROH is an alcohol. For coordinatively saturated metals in the absence of catalyst, hydrolysis and condensation, both occur by nucleophilic substitution (S_N) mechanisms. Nucleophilic substitution is a fundamental class of substitution reactions in which an “electron rich” nucleophile selectively bonds with or attacks the positive or partially positive charge of an atom attached to a group or atom called the leaving group. There are two main mechanisms, the S_{N1} reaction and the S_{N2} reaction. S stands for chemical substitution, N stands for nucleophilic, and the number represents the kinetic order of the reaction. In the S_{N2} reaction, the addition of the nucleophile and the elimination of the leaving group take place simultaneously. S_{N2} occurs when the central atom is easily accessible to the nucleophile. By contrast the S_{N1} reaction involves two steps. S_{N1} reactions tend to be important when the central atom of the substrate is surrounded by bulky groups, because such groups interfere sterically with the S_{N2} reaction. The nucleophilic addition reaction is an addition reaction in which a nucleophile is added to, followed by the removal of the leaving group and the creation of two new covalent bonds.

The reaction taking place is shown below:



Depending on the amount of water and catalyst present, hydrolysis may go to completion so that all of the OR groups are replaced by OH, or stop when the metal is only partially hydrolyzed, e.g. $\text{Si(OR)}_{4-n}(\text{OH})_n$. The thermodynamics of hydrolysis, are governed by the strength of the entering nucleophile, the electrophilicity of the metal, and the partial charge and stability of the leaving group.

pH

As mentioned above, hydrolysis is affected by the solution pH. The process is divided into three pH domains : below pH 2, pH 2-7 and above pH 7. However, regardless of the pH, hydrolysis occurs by the nucleophilic attack of the oxygen contained in water on the metal atom.

Figure 1 shows the effect of the pH on the hydrolysis rate.

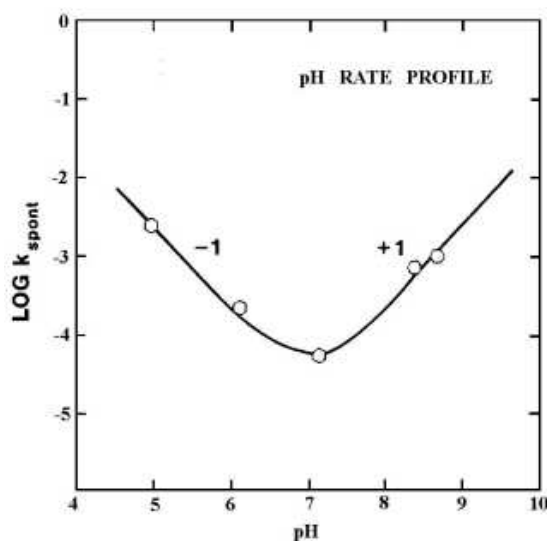


Figure 1. pH rate profile of the hydrolysis reaction

Role of the catalyst

Although hydrolysis can occur without the addition of an external catalyst, it is more rapid and complete when they are employed. The nature of the catalyst may be acidic or basic. The most generally used catalysts are mineral acids (HCl) and ammonia. Some others are acetic acid, KOH, amines, KF, and HF. It has been observed that the rate and extent of the hydrolysis reaction is mostly influenced by the strength and concentration of the acid or basic catalyst.

a. Acid-Catalyzed Mechanism

All strong acids behave similarly, although weaker acids require longer reaction times to achieve the same extent of reaction. Acids serve to protonate negatively charged alkoxide groups, enhancing the reaction kinetics by producing good leaving groups and eliminating the requirement for proton transfer within the transition state. Alkoxide groups are protonated in a rapid first step. In this way, the electron density

is withdrawn from the metal atom, making it more electrophilic and thus more susceptible to attack from water. This concludes on the formation of a penta coordinate transition state with significant S_N2 type character. This can be seen in figure 2.

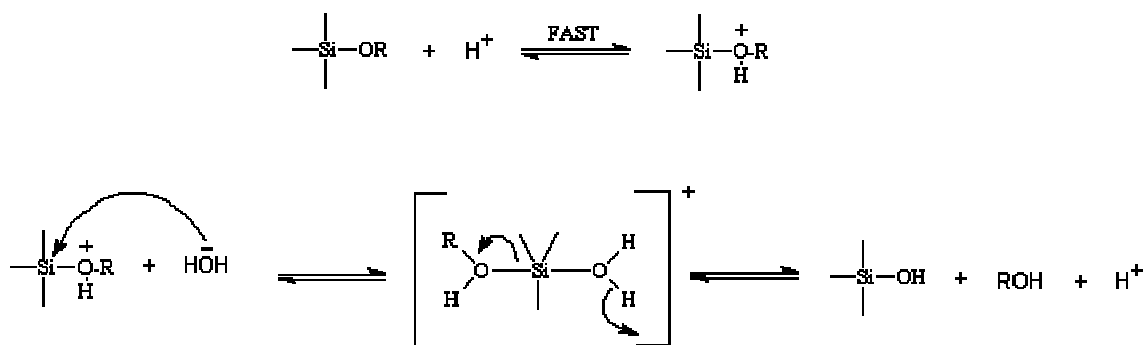
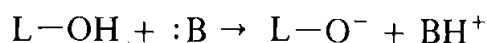


Figure 2. Acid-Catalyzed Hydrolysis

Hydrolysis goes to completion when sufficient water is added.

b. Base Catalyzed Mechanism

Base catalyzed hydrolysis proceeds much more slowly than the acid catalyzed process, at an equivalent catalyst concentration. Alkaline conditions produce strong nucleophiles via deprotonation of the hydroxo ligands:



where L = M and B = OH⁻ or NH₃. Basic alkoxide oxygens tend to repel the nucleophile, -OH. However, once an initial hydrolysis has occurred, the following reactions proceed stepwise, with each subsequent alkoxide group removed more easily from the monomer than the previous one. Although hydrolysis in alkaline environments is slow, it still tends to be complete and irreversible. Thus, under these conditions it is more likely that water dissociates to produce hydroxyl ions in a rapid first step. The hydroxyl anion then attacks the metal atom. Again, an S_N2 nucleophilic reaction has been proposed in which the -OH displaces the -OR group, as seen in figure 3.

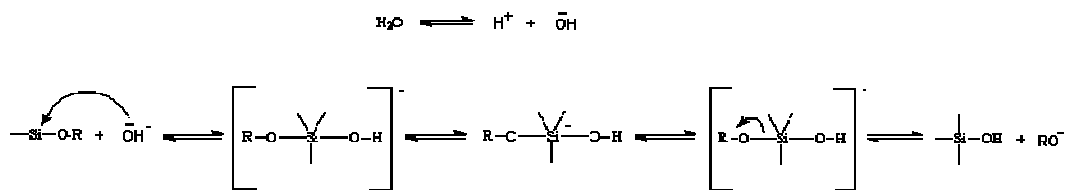
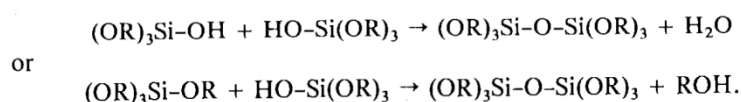


Figure 3. Base-Catalyzed Hydrolysis

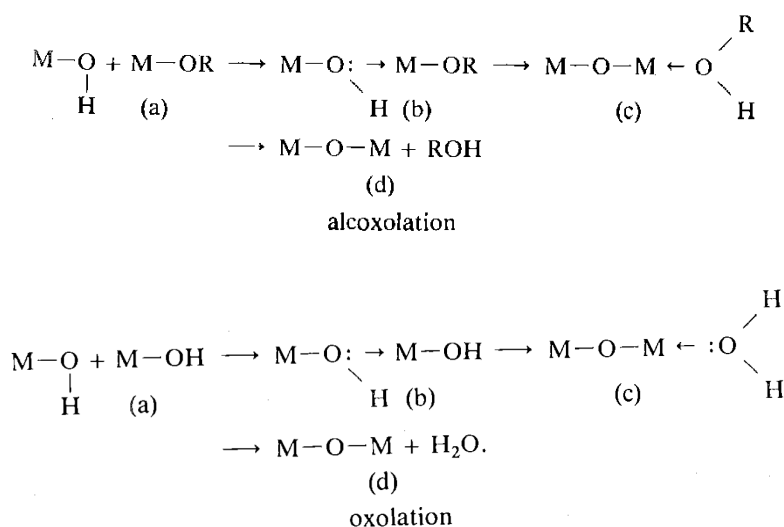
1.1.2 Condensation

Two partially hydrolyzed molecules are linked together, in a process called condensation reaction. By definition, condensation liberates a small molecule, such as water or alcohol:

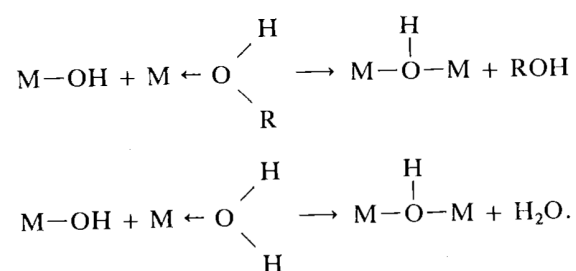


This type of reaction can continue to build larger and larger metal containing molecules. As the number of metal bonds increases, the individual molecules are bridged and jointly aggregate in a sol. When the sol particles aggregate, or inter-knit into a network, a gel is formed. Upon drying, trapped volatiles, such as water, alcohol etc, are driven off and the network shrinks as further condensation can occur.

More specifically, during condensation, nucleophilic mechanisms such as S_N and A_N take place, followed by proton transfer from the attacking molecule to an alkoxide or hydroxo-ligand within the transition state and removal of the protonated species as either alcohol (alcoxolation) or water (oxolation):



There is also a possibility that condensation can occur by olation:



The thermodynamics of alkoxolation, oxolation and olation depend on the same factors mentioned above for the hydrolysis reaction, and among which are: the strength of the entering nucleophile and the electrophilicity of the metal.

Under most conditions, condensation commences before hydrolysis is complete. However, conditions such as, pH and catalyst can force completion of hydrolysis before condensation begins.

pH

When condensation takes place at pH below 2, the rates are proportional to the $[\text{H}^+]$ concentration. It is generally agreed that between pH 2 and pH 6 condensation rates are proportional to $[\text{OH}^-]$ concentrations. Condensation preferentially occurs between more highly condensed species and those less highly condensed. This suggests that the rate of dimerization is low, however, once dimers form, they react preferentially with monomers to form trimers, which in turn react with monomers to form tetramers. Above pH 7, condensation occurs as in the pH 2 to 6 range. However, at this pH range, condensed species are ionized and therefore, mutually repulsive. Growth occurs primarily through the addition of monomers to the more highly condensed particles rather than by particle aggregation. Growth stops when the difference in solubility between the smallest and the largest particles becomes indistinguishable. Additionally, in this pH range, the growth rate depends upon the particle size distribution. The dissolution rate and relative gel time as a function of pH can be seen in figure 4.

1.1.3 Hybrid sol-gel materials

Recent technological breakthroughs and the desire for new functions generate an enormous demand for novel materials. Since ~ 1992, two types of completely new composite materials have appeared and sol-gel has been used as the route to synthesize them. These types of materials are organic-inorganic materials and do not exist in nature.

As mentioned above, new materials are synthesized by combining organic and inorganic components. Such materials are termed hybrid materials. A hybrid material is a material that includes two moieties blended on the molecular scale [2]. Commonly one of these compounds is inorganic and the other one organic. A more detailed definition distinguishes between the possible interactions connecting the inorganic and organic species. Class I hybrid materials are those that show weak interactions between the two phases, such as van der Waals, hydrogen bonding or weak electrostatic interactions. Class II hybrid materials are those that show strong chemical interactions between the components. In addition to the bonding characteristics structural properties can also be used to distinguish the various types of hybrid materials. An organic moiety that contains a functional group, can act as a network modifying compound because in the final structure the inorganic network is modified by the organic group.

The most obvious advantage of inorganic-organic hybrids is that they can favorably combine the often dissimilar properties of the organic and inorganic components in one material. Because of the many possible combinations of their components this field is very creative, since it provides the opportunity to invent an almost unlimited set of new materials with a large spectrum of known and as yet unknown properties.

The, sol-gel process is one of the modern methods employed for preparing novel inorganic-organic materials from molecular precursors[3]. The molecular precursors of the organic moiety may be monomers, which when blended with photosensitive molecules can give polymerizable resins. These photosensitive sol-gel materials are effective for the fabrication of 3D structures using the two photon polymerization technique [4], [5].

1.2 Two Photon Polymerization

2-photon polymerization (2PP) induced with a femtosecond laser, has emerged as a new microscale fabrication technology. In particular, 2PP is a very attractive three dimensional rapid microstructuring technology. Photopolymerization refers to the process of using light as an energy source to induce the conversion of small unsaturated molecules in the liquid state to solid macromolecules through polymerization reactions [6]. 2PP has many advantages as a technique for the fabrication of complex 3D structures on a scale of several microns, which are difficult to obtain using conventional miniaturization technologies. It is known that when a femtosecond laser pulse is focused into the volume of a photosensitive material, this pulse initiates two photon polymerization via a two photon absorption (TPA) process.

1.2.1 Two photon absorption

The probability of n-photon absorption is proportional to the n^{th} power of the photon flux density. Thus, high photon flux densities are required in order to observe this phenomenon. These high intensities are only provided by a laser source. The general idea is that an atom can absorb two or more photons simultaneously, allowing electron transition to higher energy states.

The theory of two photon absorption (TPA) was first developed by Maria Coppert-Mayer in 1931 and was experimentally observed for the first time in 1961 with the invention of lasers. TPA is a multiple photon excitation approach used in the initiation of photochemical changes. Most photosensitive resins that polymerize under UV (λ) exposure can undergo similar reactions when two photons (2λ) are absorbed, provided that the light intensity is high enough. Two mechanisms have been reported for TPA (see Figure 5) [7]:

- (a) stepwise excitation and
- (b) simultaneous two photon excitation

The former relies on the existence of a real intermediate state, from which an excited electron is further pumped to a higher energy level by absorbing photons of the same energy as that at the ground state. Such a process is termed stepwise TPA. Compared to simultaneous TPA, stepwise TPA doesn't require coherence of the incident light, and can be considered as two sequential single photon absorption phenomena.

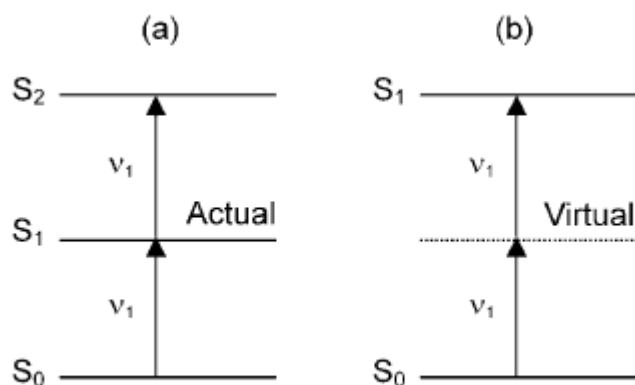


Figure 5.Mechanism of TPA

In simultaneous TPA, there is no real intermediate state, but a virtual intermediate state is created by the interaction of the absorbing species with the first photon. In this case, two photons each with half the energy of the gap between the two energy levels, induce the electron transition. Only if the second photon arrives within the virtual state lifetime, about 10^{-15} sec, can it be absorbed. Thus, it is apparent that higher intensities are required for the simultaneous TPA, which usually requires femtosecond lasers. For femtosecond laser micro-fabrication, simultaneous TPA is more relevant. For this reason, from now on any reference to TPA will refer to simultaneous TPA.

1.2.2 Mechanism of Two Photon Polymerization

TPA can be utilized for inducing photopolymerization. Two-photon polymerization was experimentally reported for the first time in 1965 by Pao and Rentzepis as the first example of multiphoton excitation-induced photochemical reactions. The difference between one photon and two photon polymerization lies in how the energy is provided. In single-photon polymerization, there is a linear response of the material to the light intensity. However, if the material response is proportional to the square of the photon density, the integrated material response is greatly enhanced at the focal point, as illustrated in figure 6.

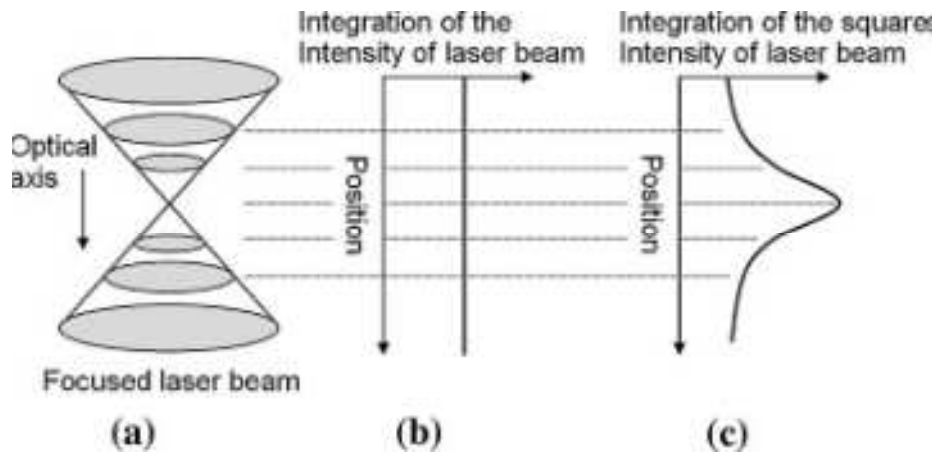


Figure 6. Comparison of TPA and to single-photon absorption generated by a tightly focused laser beam. (Maruo S, Kawata S. *Microelectromech S.* 1998; 7: 411)

The two photon transition rate is extremely small, so a very high spatial resolution can be obtained (see figure 7) [8].

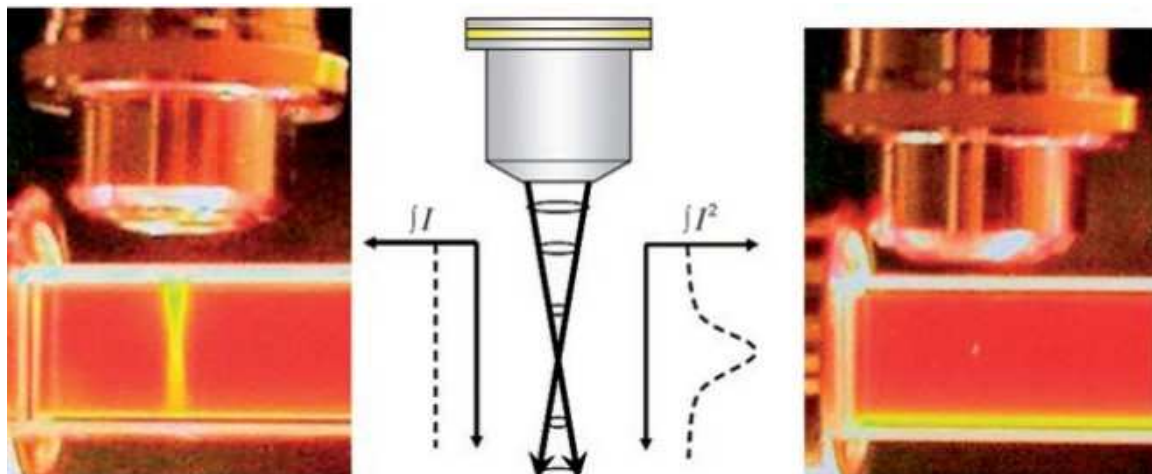


Figure 7. The laser beam in single-photon polymerization (left), and two-photon polymerization (right)

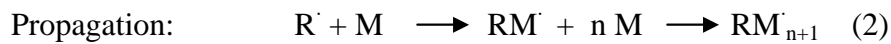
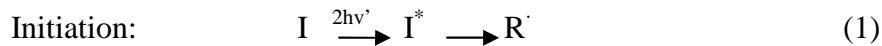
The intensity distribution of the laser beam, which is assumed to be Gaussian (figure 6(c)), is expressed by the following equation:

$$I(r_0,0) = I_0 \exp (- 2r_0^2/\omega_0^2)$$

where, r_0 , I_0 , and ω_0 are the radius of the beam, the beam intensity at the central axis in the focus plane, and the radius of the focused beam spot, respectively.

When a laser beam of high intensity is focused into the volume of a liquid photosensitive material that is transparent to NIR light, the photoinitiator that is used

to enhance two photon activation is excited by the simultaneous absorption of two photons, and results in the generation of free radicals (initiation). This is the beginning of a free radical polymerization process. The radicals formed react with monomers, producing monomer radicals which participate in a chain reaction (propagation). This reaction will continue until the monomers are consumed, or until two growing radicals meet (termination). This procedure is described with equations 1-3 [9].



or



Where $\nu' \sim \nu/2$ denotes photon frequency in the two photon excitation beam. I is the initiator, $R\cdot$ the free radical and M the monomer unit. I^* represents an excited state of the photoinitiator after absorbing the photon energy, respectively.

The density of radicals (ρ) produced by femtosecond laser pulses in the polymerization process varies with the square of the beam intensity:

$$\theta\rho/\theta t = (\rho_0 - \rho) \delta I^2$$

where, δ is the effective two photon cross-section for the generation of radicals.

1.2.3 Applications of 2-Photon Polymerization

Despite the fact that 2PP is a relatively new technology its application fields have been rapidly expanding in the recent years. Because of the high optical quality that can be achieved with 2PP, many of the applications demonstrated to date have been in the field of photonics [10]. Photonic structures include waveguides, couplers, interferometers, microlenses and even microlasers [11], [12]. Apart from that, 2PP is also used for the fabrication of micromechanical systems, microfluidic devices, biomedical devices and scaffolds for tissue engineering [13], [14], [15].

Two Photon Polymerization is a novel technique for processing hybrid organic-inorganic materials. This innovative method for 3D structuring of structural and functional materials, using fs-pulsed NIR lasers, has distinct benefits. First of all, the achievable feature resolution of about 100 nm is about one order of magnitude better than other methods such as μ -stereolithography. Furthermore, due to the non-linear process it is possible to directly write inside a given volume (“real” 3D writing), since the polymerization only takes place inside the focus of the laser beam. Therefore, complex 3D structures can be inscribed into a suitable matrix material and/or a resin which is selectively cured. These advantages perfectly fulfill the demands for various future applications requiring three dimensional structures with resolutions in the (sub)micrometer range, such as different mechanical, electronic and optical micro-devices, polymer based optical waveguides on integrated circuit boards and bio-inspired architectures.

One of the first and most thoroughly studied applications of 2PP is the fabrication of 3D photonic crystals (see figure 8) [16]. A photonic crystal is an artificial structure exhibiting periodic variation of the dielectric constant of the material. Such a structure has a similar effect on the propagation of photons, as the periodic variation of electric potential in regular crystals on propagating electrons, hence the name of photonic crystal.

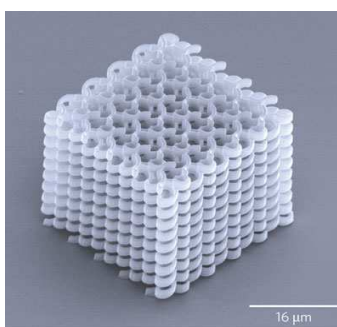


Figure 8. Spiral photonic crystal.

One of the most popular approaches of 2PP in tissue engineering is the fabrication of 3D scaffolds whose function is to guide and support cell proliferation in 3D [17]. The ability to produce arbitrary 3D scaffolds is therefore very appealing. The 2PP technique can also be applied for the fabrication of implants and prostheses. The materials used for these purposes must demonstrate appropriate biological compatibility, stability and stiffness. The versatility of the 2PP technology and the

large number of applicable materials contribute to the wide range of applications of this technology which are rapidly growing.

Great interest has been focused recently to 3D luminescent devices with micrometer size [18]. These devices can be fabricated by 2PP from semiconductor-polymer composites. The semiconductor nanoparticles in the materials show unique tunable light emission properties, arising from quantum size effects.

1.3 Quantum Dots

Quantum dots are nanoparticles of semiconductor crystals. They sound very exotic and indeed they are, in terms of the way they work, which is dictated by the rules of quantum mechanics. The term “quantum dot” was first coined by the physicist Mark Reed in the late 1980s in an effort to describe the strange way in which mighty small semiconductor crystals seem to take on the characteristic properties of both bulk materials and discrete atoms

Quantum dots have the unique property of having a very narrow emission spectrum, which is directly proportional to their particle size [19]. They absorb light efficiently and respond by emitting at a very specific wavelength. Their size fluctuates between 1 and 12 nm in diameter, which includes 10-50 atoms, and the charge carriers in these systems, which are electrons or holes, can only occupy a restricted set of energy levels, just like the electrons in an atom. This is the reason why quantum dots have been called artificial atoms. At these small sizes materials behave differently, giving quantum dots unprecedented tunability and enabling their novel applications to science and technology. The size of the particle is very important because its optical properties depends on that [20]. The smaller the size of the particle the more its emission becomes blue shifted and conversely the larger the particle, the more its emission is red shifted. This phenomenon, allows emission of the complete light spectrum from the same material, by simply controlling the particle size (figure 9).

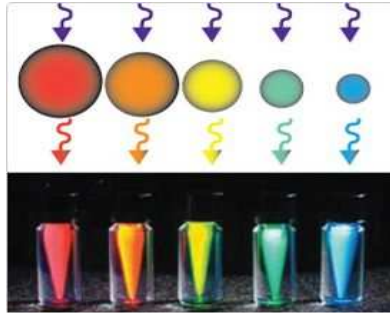


Figure 9. Nanocrystal solutions excited with the same UV lamp. The size of the nanocrystal determines the emitted color.

1.3.1 How Quantum Dots work

In order to understand how quantum dots work, bulk semiconductors should be first understood. In bulk semiconductors the energy levels, that the electrons occupy, are very close to each other and they can be described as continuous. That means that there is almost no energy difference between them. There is also a region of forbidden electron energies that is called the bandgap. This energy bandgap is different for each bulk material. The energy levels below the bandgap are called valence band and the energy levels above the bandgap are called conduction bands. A very small amount of electrons occupy the conduction band and the majority of them occupy the valence band, filling it almost completely. There is a possibility that an electron can jump to the conduction band, if it acquires enough energy to cross the band gap. This can be accomplished by applying a stimulus such as heat, voltage or photon flux. When an electron “jumps” to the conduction band, a vacation is created at the valence band. This vacation is referred as a hole since it leaves a temporary “hole” in the valence band electron structure. This hole is positively charged due to the absence of the electron. The raised electron and the hole, taken as a pair are called an exciton. When an electron falls down across the bandgap to the valence band, electromagnetic radiation is emitted with wavelength that corresponds to the energy it loses. Because the energy bandgap of the bulk semiconductors is fixed, the emission frequencies of the electron transitions are also fixed. Quantum dots offer the unnatural ability to tune the bandgap and as a result the emission wavelength [21].

In quantum dots, the electrons have a range of energies. There is a physical separation between the electron and the hole, which is called Exciton Bohr Radius. This distance is different in each material. The dimensions of bulk semiconductors are much larger than the Exciton Bohr Radius. When the size of the quantum dots approaches the size

of the Exciton Bohr Radius the electron energy levels are treated as discrete. This situation of discrete energy levels is called quantum confinement. This has large repercussions on the absorptive and emissive behavior of the semiconductor material.

The addition or subtraction of just a few atoms in the quantum dot can alter the boundaries of the bandgap. The bandgap in a quantum dot is energetically larger, as the size of the dot decreases, thus, the radiation from the quantum dot is “blue shifted” compared to the bulk material as well as to bigger sized quantum dots.

1.3.2 Quantum dot nonlinear optical effect

Another very interesting property that quantum dots exhibit, is that of third order optical nonlinearity. There are two major categories that fall into this order of nonlinearity: frequency mixing (e.g. Third-Harmonic Generation) or intensity dependent refractive index [22]. The later provides a basis for all optical processing of information, which could result in tremendous gain in speed and is the subject of study in this thesis.

When light propagates through a medium, the applied electric field of light polarizes the molecules of the medium, displacing them from their equilibrium positions and induces a dipole moment μ_{ind} given by

$$\mu_{\text{ind}} = -er$$

where, e is the electronic charge and r is the field induced displacement. The polarization of the medium due to this induced dipole is given by

$$P = -Ner$$

where, N is the electron density in the medium. This polarization opposes the externally applied field and results to a lower electric field inside the material. The polarization is often expressed in terms of susceptibility $\chi^{(n)}$ as

$$P = \chi^{(1)} \cdot E + \chi^{(2)} : EE + \chi^{(3)} : EEE + \dots$$

or

$$P = \chi_{\text{eff}} E$$

The coefficient $\chi^{(1)}$ is the linear susceptibility whereas the coefficient $\chi^{(2)}$ relating the polarization to the square of the electric field strength E is called the second order nonlinear susceptibility of the medium and its magnitude describes the strength of second order processes. The $\chi^{(3)}$ term is referred to as second nonlinear susceptibility describing third-order processes. Similarly, higher order terms describe higher order processes. For most materials, these higher order effects are very difficult to observe, so we limit our discussion up to and including third order effects. The second expression of polarization is analogous to the first, except that χ_{eff} is now dependent on the field strength.

The interaction of light with a medium is fully described by Maxwell's equation. The wave equation describing the propagation of an electromagnetic wave is

$$\nabla^2 E = -\frac{\epsilon}{c^2} \frac{\partial^2 E}{\partial t^2}$$

where, c is the speed of light, ϵ is the dielectric constant and ∇^2 is the Laplace operator which is defined as

$$\nabla^2 = \frac{\partial^2}{\partial x^2} + \frac{\partial^2}{\partial y^2} + \frac{\partial^2}{\partial z^2}$$

The above equation relates the time and space variations of the electric field of light through the materials response, specified by the dielectric constant ϵ , and is of fundamental importance in understanding the interaction of field with the medium. An example, is light propagating as a plane wave in the z direction. Then the Maxwell's equation simplifies to

$$\frac{\partial^2 E}{\partial z^2} = -\frac{\epsilon}{c^2} \frac{\partial^2 E}{\partial t^2}$$

A solution for the above equation, is a sinusoidal oscillation

$$E(z, t) = E^{(0)} \cos(\omega t - kz)$$

with

$$k^2 = \frac{\epsilon \omega^2}{c^2}$$

and with $E^{(0)}$ defining the amplitude of the field. The term k is the propagation constant in the material and is equal to 2π times the number of waves per unit length

$$k = \frac{2\pi}{\lambda}$$

The quantity k is a vector called propagation vector. It characterizes the phase of the optical wave with respect to a reference point ($z = 0$, for instance) and kz describes the relative phase of the wave.

Substituting the solution of the Maxwell's equation into the polarization expansion equation gives

$$P = \chi^{(1)}E_0 \cos(\omega t - kz) + \chi^{(2)}E_0^2 \cos^2(\omega t - kz) + \chi^{(3)}E_0^3 \cos^3(\omega t - kz)$$

Using the appropriate trigonometric identities for $\cos^2 \theta$ and $\cos^3 \theta$ gives

$$P = \chi^{(1)}E_0 \cos(\omega t - kz) + \frac{1}{2}\chi^{(2)}E_0^2 [1 + \cos(2\omega t - 2kz)] \\ + \chi^{(3)}E_0^3 \left[\frac{3}{4}\cos(\omega t - kz) + \frac{1}{4}\cos(3\omega t - 3kz) \right]$$

The above equation shows the presence of new frequency components due to the non linear polarization. The second order term gives a frequency independent contribution as well as one at 2ω and corresponds to second-harmonic generation. The third term indicates a frequency response at the frequency of the optical field ω as well as at 3ω which refers to the third-harmonic generation.

Another manifestation of nonlinear optic is the so-called nonlinear index of refraction of the medium. The refraction index (n) is another way of representing the optical response of a medium. For an isotropic medium

$$n^2 = 1 + 4\pi\chi_{eff}$$

When a medium is subjected to a dc electric field, which we designate as $E(0)$, and an optical field $E(\omega)$, the total field of the medium is

$$E = E(0) + E(\omega) = E(0) + E_0 \cos(\omega t - kz)$$

Substituting to the polarization expansion equation gives

$$P = \chi^{(1)}[E(0) + E_0 \cos(\omega t - kz)] + \chi^{(2)}[E(0) + E_0 \cos(\omega t - kz)]^2 + \chi^{(3)}[E(0) + E_0 \cos(\omega t - kz)]^3 + \dots$$

Expanding these terms, applying the appropriate trigonometric identities, and collecting terms that describe oscillation ω gives

$$\begin{aligned} P(\omega) &= \chi^{(1)}E_0 \cos(\omega t - kz) + 2\chi^{(2)}E(0)E_0 \cos(\omega t - kz) \\ &+ 3\chi^{(3)}E_0^2 \cos(\omega t - kz) + \frac{3}{4}\chi^{(3)}E_0^3 \cos(\omega t - kz) \\ &= \chi_{eff} E(0) \cos(\omega t - kz) \end{aligned}$$

Substituting χ_{eff} to the refraction index equation, results

$$n^2 = 1 + 4\pi[\chi^{(1)} + 2\chi^{(2)}E(0) + 3\chi^{(3)}E^2(0) + \frac{3}{4}\chi^{(3)}E_0^2]$$

By replacing $n_0^2 = 1 + 4\pi\chi^{(1)}$, which corresponds to the linear index of refraction, gives

$$n = n_0 + \frac{4\pi\chi^{(2)}}{n_0}E(0) + \frac{6\pi\chi^{(3)}}{n_0}E(0)^2 + \frac{3\pi}{2n_0}\chi^{(3)}E_0^2$$

The definition of the light intensity in cgs units is:

$$E_0^2 = \frac{8\pi}{cn}I(\omega)$$

which when substituted to the above equation of the index of refraction gives

$$n = n_0 + \frac{4\pi\chi^{(2)}}{n_0}E(0) + \frac{6\pi\chi^{(3)}}{n_0}E(0)^2 + \frac{12\pi^2}{cn_0^2}\chi^{(3)}I$$

where,

$$\frac{4\pi\chi^{(2)}}{n_0} = n_1$$

$$\frac{6\pi\chi^{(3)}}{n_0} = n_2(0)$$

$$\frac{12\pi^2}{cn_0^2}\chi^{(3)} = n_2(\omega)$$

and correspond to the linear electrooptic effect, the quadratic electrooptic effect, and the optical Kerr effect, respectively. The later corresponds to the light intensity-dependent refractive index.

When light passes through a semiconductor, the material absorption creates excitations, the so called excitons, which are electron-hole pairs. The concentration of excitons will depend on light intensity. The refractive index of the material is dependent on the concentration of the optically generated excitations. Consequently, the refractive index will depend on intensity [23]. This population effect describes a $\chi^{(3)}$ process, which is a measure of the intensity dependent refractive index. Such a process though, cannot contribute to third-harmonic generation and thus constitutes a fundamentally different type of effect. This resonant $\chi^{(3)}$ is sometimes called dynamic nonlinearity or incoherent nonlinearity, because it depends on the excited state population, and its response time is determined by the dynamics of the population decay. If for a material the absorption to an excited state is intensity dependent, the change in absorption $\Delta\alpha$ as a function of intensity gives rise to a change in refractive index Δn by the Kramers-Kroening relation as follows

$$\Delta n(\omega) = \frac{c}{\pi} p. v. \int_0^{\infty} \frac{d\omega' \Delta\alpha(\omega')}{\omega'^2 - \omega^2}$$

This equation is often used for the calculation of Δn and $\chi^{(3)}$. The mechanisms that give rise to the intensity dependence of absorption are the following:

Saturable Absorption. Materials processing strong electronic absorptions can behave as saturable absorbers as long as the rate of populating the excited states exceeds the rate of return to the ground state. As the excited states are populated, there is a corresponding depletion of the ground state population, which leads to a decrease in the absorption involving transition from the ground state. Consequently, the absorption saturates at higher intensities. The result is an intensity dependent absorption.

Phase-Space Filling. This is a special case of saturation of ground state absorption originally proposed for multiple-quantum well semiconductors. In these systems, the lowest energy excitation produces excitons, which are correlated electron-hole pairs. These excitons have a certain geometric size corresponding to the average separation

between the electron and hole. At low excitation densities, the excitons behave like bosons (neutral particles). At higher excitation densities, the excitonic separation approaches the geometric size of excitons. At this excitation density, excitons no longer behave like bosons, and the fermion nature (charged particle repulsion) of electron-hole pair now becomes manifested in blocking further photogeneration of excitons. This is called the space filling of excitons, which results to the reduction of the absorption length. The result is an intensity dependent absorption, which, according to Kramers-Kroening relation, leads to an intensity dependent refractive index and hence $\chi^{(3)}$.

This intensity dependent refractive index leads to a special case of processes, the so called self-action effects. It is called self-action effect since the nonlinear polarization created by an incident beam affects the propagation of other properties of the same beam through an intensity dependent refractive index. These types of effects are:

Self-focusing, which occurs as a combined result of positive n_2 , and a spatial variation of the laser intensity, in which the beam is more intense in the center than at the edges. The result is that the refractive index of the nonlinear medium in the center of the beam is larger than at the edges and the medium acts as a positive lens focusing the beam.

Self-defocusing, which results when n_2 is negative. In this case the spatial variation of the laser intensity creates a negative lens resulting in defocusing of the beam.

Self-phase modulation, which is associated with the temporal behavior of the induced refractive index change, $\Delta n(t) = n_2 I(t)$, and is important only when the optical pulse is of the order of a picosecond or less. The result is broadening of the frequency profile.

1.3.3 Quantum dot - polymer composites

Composites consisting of a polymer matrix filled with nanosized particles are of great interest because of their long-term stability and because they offer new strategies for influencing interactions that may take place between the matrix and the nanoparticles. These composites are promising materials for the new generation of optical and electronic devices and for biological labeling [24].

The incorporation of quantum dots into polymer matrices has been a subject of intense research efforts. One of the challenges involved in the preparation of such materials is the incompatibility of the quantum dots with the polymer matrix.

Recently great interest has been paid to 3D luminescent polymeric devices; however, not much research has been carried out in this field due to the difficulty of manufacture such structures. To realize 3D microstructures of luminescent polymer nanocomposites, it is essential to develop a suitable method for the fabrication of 3D structures from polymer nanocomposites with embedded nanoparticles. This approach will enable the fabrication of tunable microstructures and the development of high efficiency polymer-based optoelectronic devices [25], [26].

1.4 Photonic crystals

Photonic crystals are periodically structured electromagnetic media, generally possessing photonic band-gaps: ranges of frequency where no light propagation is allowed through the structure [27]. The periodicity of such structures is proportional to the wavelength of light in the band-gap. Photonic crystals can be treated as the electromagnetic analogue of a crystalline atomic lattice that acts on the electron wavefunction to produce the familiar energy band gaps. For example semiconductors have a complete band-gap between the conduction and the valence energy bands. The optical analogue is the photonic crystal, in which the atoms or molecules are replaced by macroscopic media with differing dielectric constants and the periodic potential is replaced by a periodic dielectric function or, equivalently, a periodic index of refraction [28].

The field of photonic crystals is a marriage of solid state physics and electromagnetism. They are called “crystals” because of their periodicity and “photonic” because they act on light. In order to get a clue of how they work, imagine shining a light through a large block of glass with a single bubble of air in it. When light strikes the bubble, some of it will reflect and some of it will continue forward at a slightly different angle (be refracted) [29]. As you look through the glass, this scattered light allows you to see the bubble. Picture now a second bubble in the glass, just like the first one, but at a different place. As before, the light will reflect and refract, this time from both bubbles. Next, suppose that we fill the glass with millions of bubbles, all identical and arranged in a perfect periodic lattice extending in all

directions. If someone would look carefully enough, he/she would discover that all of these reflections and refractions cancel one another before reaching our eyes, and the light passes through the crystal unimpeded. This is no accident, but a general consequence of the periodicity of the structure. Light waves, like all waves, can interfere and even cancel if they superimpose. At this part, it is helpful to mention Bloch's or Floquet's theorem, which says that, in a periodic medium, waves can be found that propagate without scattering, and this is equally true whether the waves consist of electrons or of light beams or sound or... . This theorem leads to many other curious phenomena, if the above bubbles (the scatterers) have period in the order of the wavelength of light and if they have the right shape. It is thus possible that all of those reflections and refractions will cancel not only the light scattered sideways, but the light moving forward as well. Then because the light has to go somewhere (energy is conserved), it has no choice but to go back, it is forbidden from entering the photonic crystal. This happens no matter what direction the light is coming from, in a certain range of wavelengths called the *photonic band-gap* [30].

Once you have such a medium, impervious to light, you can manipulate photons in many interesting ways. By carving a tunnel through the material, you have an optical wire from which no light can deviate. By making a cavity in the center of the crystal, you have an optical "cage" in which a beam of light could be caught and held. These kinds of abilities to trap and guide light have many potential applications in optical communications and computing, where we would like to make tiny optical "circuits" to help manage the ever-increasing traffic through the world's optical communication networks. Other potential devices that can be fabricated from this control over light are: more efficient lasers and LED light sources and cellular phones that don't pump half of their signal power into your head.

CHAPTER 2

EXPERIMENTAL

2.1 Materials

The material was prepared using methacryloxypropyltrimethoxysilane (MAPTMS, Polysciences Inc.), Cadmium methacrylate $\text{Cd}(\text{MA})_2$, 2-(dimethylamino)ethyl methacrylate (DMAEMA, Sigma-Aldrich) and methacrylic acid (MAA, Sigma-Aldrich). Zirconium propoxide $\text{Zr}(\text{OPr})_4$, (ZPO, 70% solution in 1-propanol, Sigma-Aldrich) was used as an inorganic network former. All chemicals were used without further purification.

The materials investigated in this work, are hybrid photosensitive materials, containing organic and inorganic moieties. Such materials have the advantage of combining the dissimilar properties of the two components, in one system. For the preparation of the materials, the sol-gel process was used. The inorganic part of these composites is derived from metal alkoxides, which upon hydrolysis and condensation, form an inorganic network. The organic part comprises monomer units which carry photopolymerizable functional groups that are attached to the inorganic network. The photosensitivity of these materials arises from the use of appropriate photoinitiators. Such molecules, when treated with specific wavelength radiation, have the ability of initiating polymerization of the organic part, resulting in the formation of an organic-inorganic network.

All materials undergo a four step process [31]:

1. Hydrolysis and condensation of the metal alkoxides or monomers, to form a porous interconnected cluster structure. These reactions are catalyzed by the presence of HCl.
2. Gelation of the material, during which any solvent present in the system, is removed by heating at low temperature. During this step, hydrolysis and condensation also occurs leading to a significant volume loss.
3. The third step involves photopolymerization. Due to the presence of vinyl monomers and the photoinitiator which generates free radicals under TPA, a free radical polymerization occurs only in the irradiated area where the radicals are present. This process results in the formation of the polymer backbone and the 3D structure fabrication.

4. The fourth and final step is the material development. At this step the material is immersed in an appropriate solvent and any unpolymersized resins are removed.

As mentioned above, the precursors used were metal alkoxide-based monomers. For the formation of the inorganic network zirconium propoxide was used. Methacryloxypropyltrimethoxysilane (MAPTMS), 2-(dimethylamino)ethyl methacrylate (DMAEMA) and methacrylic acid (MAA) served as the hybrid and organic monomers. MAPTMS carries a trialkoxysilane functional group, which can undergo hydrolysis and condensation and is thus attached to the inorganic network while, bearing a polymerizable methacrylate moiety as well. Cadmium methacrylate ($\text{Cd}(\text{MAA})_2$) was used as the precursor for the formation of the CdS nanoparticles. As photoinitiator, 4,4' – Bis(diethylamino) benzophenone (BIS) was used. Figure 1 shows the chemical formulas of the above molecules.

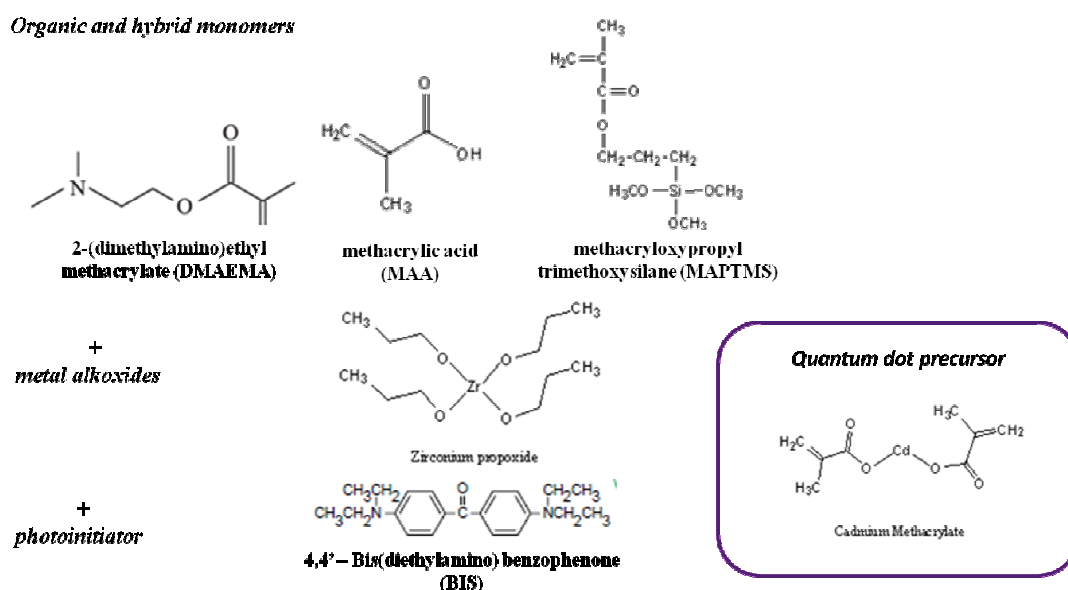
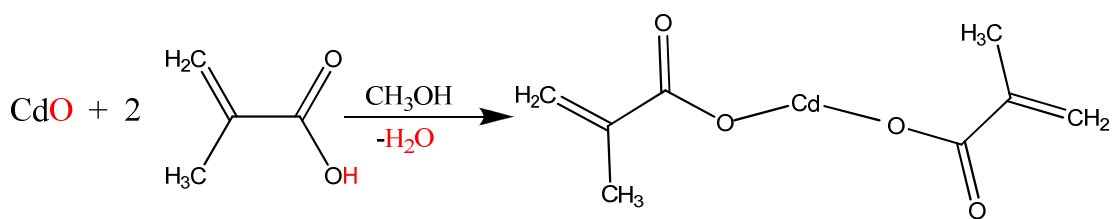


Figure 1. Chemical formulas of the precursor molecules used for the synthesis of the hybrid materials.

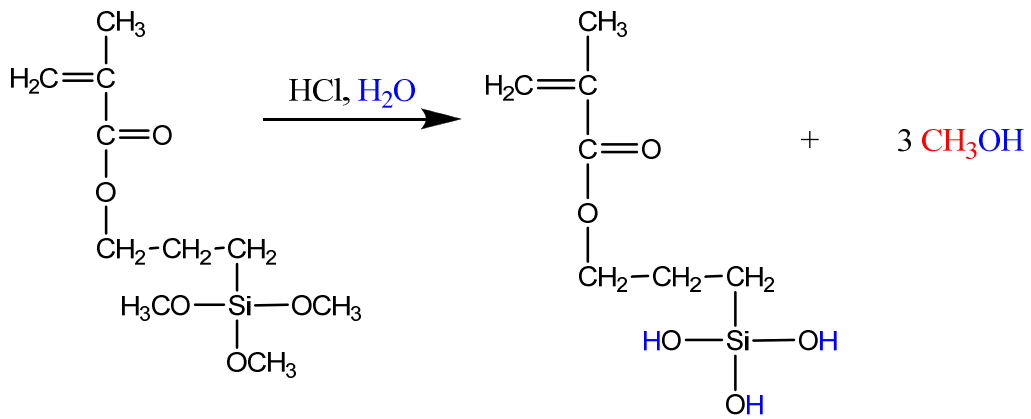
2.2 Synthesis of the material

First, $\text{Cd}(\text{MA})_2$ was prepared as following [32]: Cadmium oxide (CdO , Sigma-Aldrich) was added in portions in a flask, containing MAA and 1,5 ml of ethanol at room temperature. The molar ratio of CdO to MAA was 1:2. Subsequently the mixture was stirred for 24 hours and the desired product was obtained:

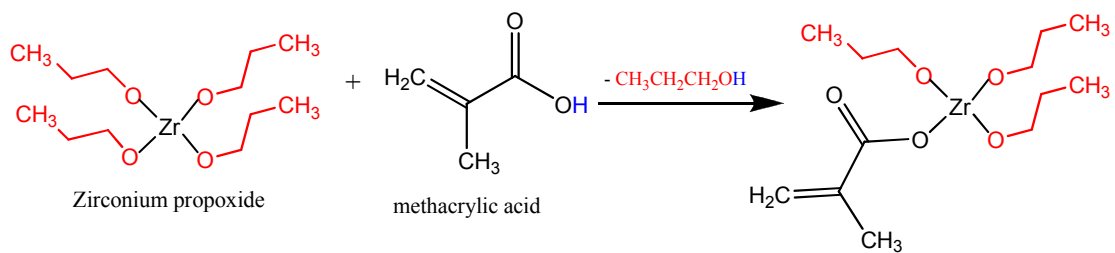


Next, MAPTMS (8:2 molar ratio as to ZPO) was hydrolyzed with the addition of HCl (concentration 0.1 M) and the mixture was stirred for 15 minutes. In a separate flask, ZPO was chelated by adding MAA at a 1:1 molar ratio. The solution was stirred for 20 minutes. The hydrolyzed MAPTMS was then added dropwise to the ZPO solution, following another 20 minutes of stirring. DMAEMA was then added, in a molar ratio 10% with respect to MAPTMS and MAA. The mixture was stirred for 5 minutes, following the subsequent addition of a small amount of nanopure water. After that, Cd(MA)₂ was added to the flask at a 1:1 molar ratio with respect to ZPO. The mixture was stirred for 30 minutes. BIS (Sigma-Aldrich), 1% w/w to the monomers, was used as the photoinitiator. After stirring for 30 minutes, the material was filtered using 0.45 μm pore size filters. Figure 2 shows the reactions described above.

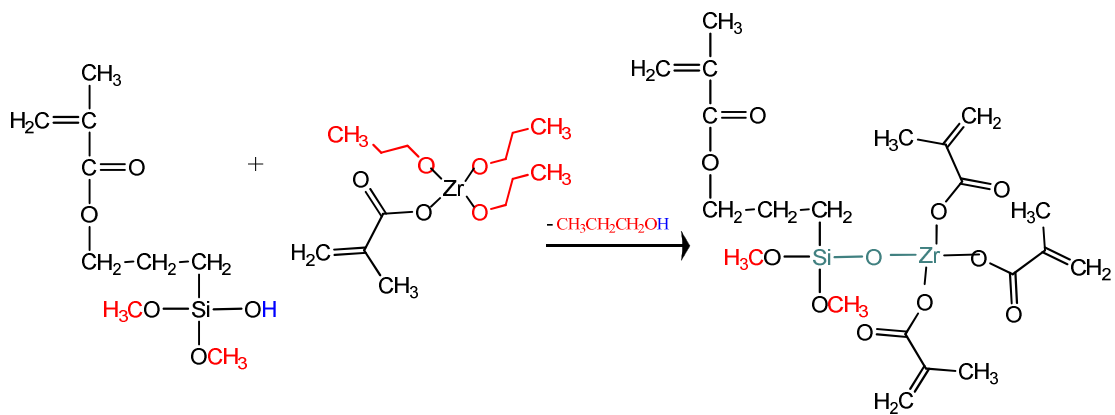
The samples were prepared by spin-coating or drop-casting (for the 3D laser microfabrication) onto thin glass substrates, and the resultant films were dried under vacuum at ambient temperature for three days before photopolymerization. The drying process resulted in the evaporation of the solvents and the condensation of the hydroxy-mineral moieties leading to the formation of the inorganic network. Next, the samples were polymerized under irradiation (laser or UV lamp), and the non-polymerized material, was removed by developing the samples sequentially in 4-methyl-2-pentanone, 2-propanol and dimethyl sulfoxide (DMSO). After the development process, the samples were immersed in a sodium sulfide (Na₂S) solution in water. The samples remained immersed for 6 hours in the solution, to form pale yellow nanocomposites. Finally they were rinsed several times with nanopure water and were allowed to dry at room temperature.



Hydrolysis of MAPTMS



Complexation of ZPO with MAA



Condensation reaction and formation of the inorganic network

Figure 2. Chemical reactions leading to the Si-Zr composite formation

2.3 3D Microfabrication

The experimental setup used for the fabrication of the 3D microstructures by two photon polymerization is shown in Figure 3.

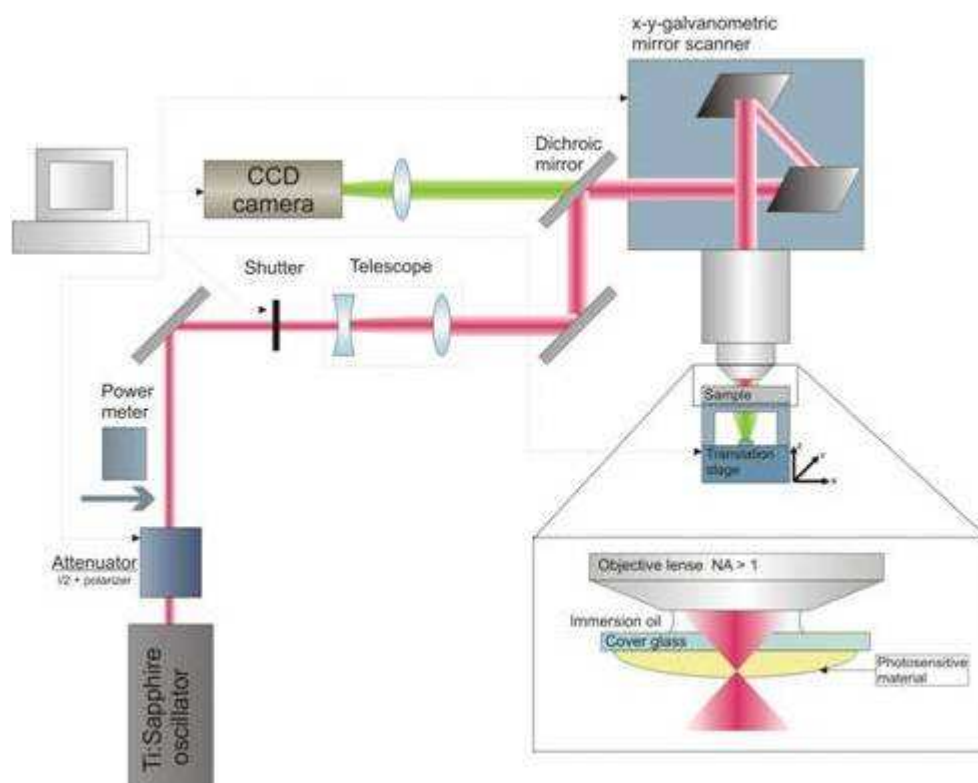
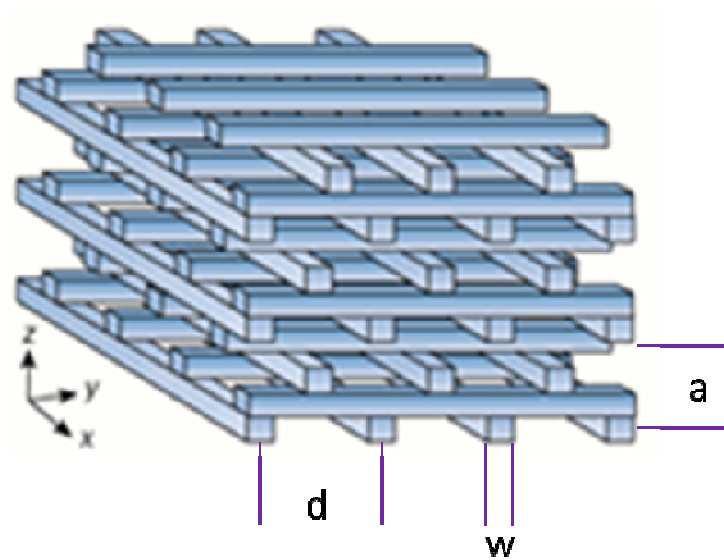


Figure 3. Experimental set-up for 2PP

The laser source was a Ti:Sapphire femtosecond oscillator operating at 800 nm. The laser pulse length was less than 20 fs with a repetition rate of 50-80 MHz. A 100X, 1.4 N.A, microscope objective lens was used to focus the laser beam into the volume of the photosensitive material. The photopolymerized structure was generated in a layer by layer process, using x-y-z piezoelectric stages (PI), controlled by 3Dpoli software. Large scale movement was achieved using a high resolution linear stage. Beam control was achieved by using a fast mechanical shutter, while beam intensity control was achieved using a combination of neutral density filters and a motorized polarizer analyser system (Altechna) waveplate. The online monitoring of the photopolymerization was achieved with a CCD camera, mounted behind a dichroic mirror. As the refractive index of the material changes during polymerization, the illuminated structure becomes visible during the fabrication process.

2.3.1 The woodpile structure

For the fabrication of the 3D microstructures the woodpile geometry was chosen (see figure 4). It consists of layers of one dimensional rods with a stacking sequence that repeats itself every four layers. The distance between four adjacent layers is “a” and within each layer, the axes of the rods are parallel to each other with a distance “d” between them. The adjacent layers are rotated by 90°. Between every other layer, the rods are shifted relative to each other by “d/2”. The ratio a/d was chosen to equal two square in order to obtain an FCC lattice.



a = distance between 4 adjacent layers
d = distance between two rods
w = thickness of the rod

Figure 4. Geometry of the woodpile structure

2.4 Characterization Techniques

Various techniques were used for the characterization of the synthesized QD hybrid material and for the three-dimensional woodpile photonic crystals. These involve: scanning electron microscopy (SEM), ultraviolet-visible spectroscopy (UV-vis), fluorescence spectroscopy, X-Ray diffraction (XRD), Z-scan, white light diffraction, and pump-probe.

2.4.1 Scanning Electron Microscopy (SEM)

SEM is a microscopy technique which uses electrons instead of light to form the image. Since its development in the early 1950's, scanning electron microscopy has developed new areas of study in the medical and physical science communities. SEM has allowed researchers to investigate a much greater variety of specimens [33], [34].

The scanning electron microscope has many advantages over traditional microscopes. It has a large depth of field, which allows a greater area of a specimen to be in focus at one time. The SEM also has much higher resolution, so closely spaced specimens can be magnified to a much greater extent. Because SEM uses electromagnets rather than lenses, the researcher has a better control of the degree of magnification. All these advantages, as well as the actual strikingly clear images, make scanning electron microscopy one of the most useful techniques in material research today.

SEM images the sample surface by scanning it with a high-energy beam of electrons in a raster scan pattern. The electrons interact with the atoms that make up the sample producing signals that contain information about the sample's surface topography, composition and other properties such as electrical conductivity. In a typical SEM, an electron beam is thermionically emitted from an electron gun fitted with a tungsten filament cathode. The electron beam, which typically has an energy ranging from a few hundred eV to 40 keV, is focused by one or two condenser lenses to a spot about 0.4 nm to 5 nm in diameter. The beam passes through pairs of scanning coils or pairs of deflector plates in the electron column, which deflect the beam in the x and y axes so that it scans in a raster fashion over a rectangular area of the sample surface (see Figure 5).

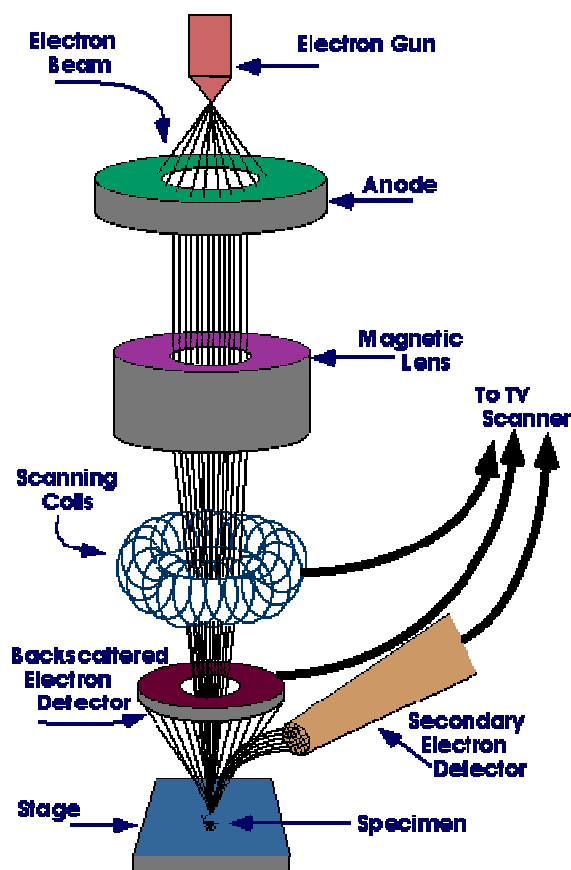


Figure 5. SEM Diagram courtesy of Iowa State University SEM Homepage

When the primary electron beam interacts with the sample, the electrons lose energy by repeated random scattering and absorption within a teardrop-shaped volume of the specimen known as the interaction volume, which extends from less than 100 nm to around 5 μm into the surface. The size of the interaction volume depends on the electron's landing energy, the atomic number of the specimen and the specimen's density. The energy exchange between the electron beam and the sample results in the reflection of high-energy electrons by elastic scattering, emission of secondary electrons by inelastic scattering and the emission of electromagnetic radiation, each of which can be detected by specialized detectors

Scanning Electron Microscopy was used for the imaging of the 3D structures. The fabricated structures were coated with a-10 nm gold (Au) film using the sputtering technique. Secondly, the characteristic X-rays produced from the specimen due to the inelastic scattering of the electron beam, were exploited in order to take EDS spectra which give information about the elements present in the 3D structures.

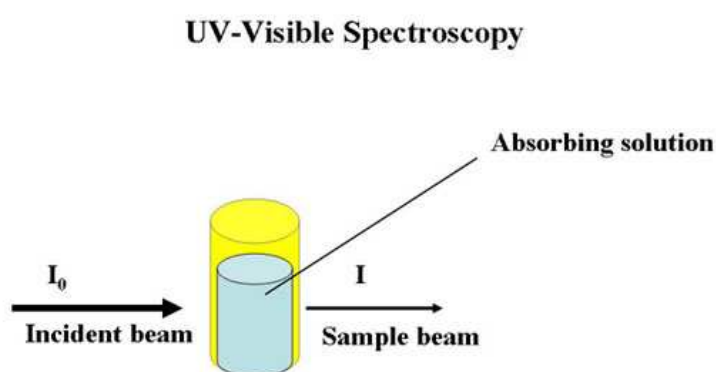
2.4.2 UV-Vis spectroscopy

Ultraviolet and visible spectroscopy (UV-Vis) is a reliable and accurate analytical technique that allows the analysis of an absorbing substance [35]. Specifically, UV-Vis spectroscopy measures the absorption, transmission and emission of ultraviolet and visible light by matter. When ultraviolet or visible light strikes atoms or molecules they can either bounce off or cause electrons to jump between energy levels.

Absorption of ultraviolet or visible light electromagnetic radiation causes electron to moves from lower energy levels to higher energy levels. UV-Vis absorption spectroscopy measures the absorption of ultraviolet or visible light by matter. Because the spectrum of an atom or molecule depends on its electron energy levels, UV-Vis absorption spectra are useful for identifying unknown substances.

The instrument used in Uv-Vis spectroscopy is called a UV/vis spectrophotometer. It measures the intensity of light passing through a sample (I), and compares it to the intensity of light before it passes through the sample (I_0). The ratio I / I_0 is called the transmittance, and is usually expressed as a percentage (%T). The absorbance, A , is defined as:

$$A = -\log(\%T / 100\%) = -\log (I/I_0)$$



- The maximum wavelength is the wavelength at which the sample absorbs the most light.
- At this wavelength, most light is absorbed so the sample beam is weakest.

2.4.3 Fluorescence Spectroscopy

Fluorescence is a spectrochemical method of analysis in which the molecules of the analyte are excited by irradiation at a certain wavelength and emit radiation of a different wavelength [36]. The emission spectrum provides information for both qualitative and quantitative analysis. When light of an appropriate wavelength is absorbed by a molecule, the electronic state of the molecule changes from the ground state to one of the many vibrational levels in the excited electronic states. Collisions with other molecules cause the excited molecule to lose vibrational energy until it reaches the lowest vibrational state of the excited electronic state. Once the molecule is in this excited state relaxation can occur via several processes. Fluorescence is one of these processes and results in the emission of light.

A spectrofluorometer is an analytical instrument used to measure and record the fluorescence of a sample. While recording the fluorescence, the excitation, emission, or both wavelengths may be scanned. The light from an excitation source passes through a filter or monochromator, and strikes the sample. A proportion of the incident light is absorbed by the sample, and some of the molecules in the sample fluoresce. The fluorescent light is emitted in all directions. Some of this fluorescent light passes through a second filter or monochromator and reaches a detector, which is usually placed at 90° to the incident light beam to minimize the risk of transmitted or reflected incident light reaching the detector (Figure 6).

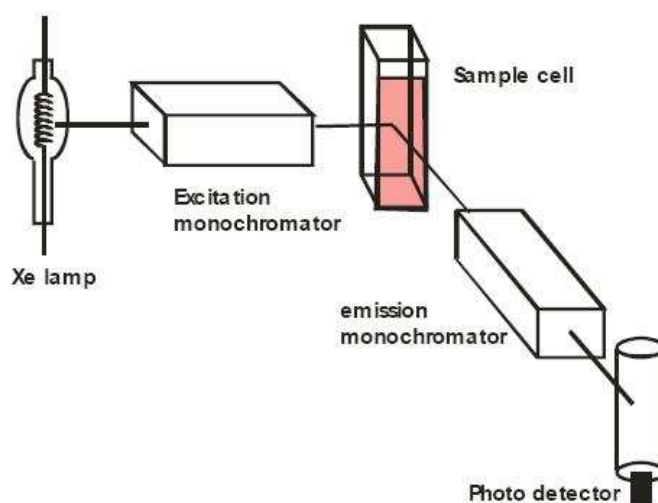


Figure 6. The fluorospectrophotometer

2.4.4 X-ray Diffraction (XRD)

X-ray diffraction is used to determine the structure of a material using X-rays [37]. X-ray diffraction techniques are based on the elastic scattering of X-rays from structures that have long range order.

Diffraction occurs as waves interact with a regular structure whose repeat distance is similar to the wavelength. The phenomenon is common in nature, and occurs across a broad range of scales. For example, light can be diffracted by a grating having scribed lines spaced in the order of a few thousand angstroms, about the wavelength of light.

It happens that X-rays have wavelengths in the order of a few angstroms, the same as the typical interatomic distances in crystalline solids. That means X-rays can be diffracted from minerals which, by definition, are crystalline and have regularly repeating atomic structures. When certain geometric requirements are met, X-rays scattered from a crystalline solid can constructively interfere, producing a diffracted beam (see figure 7).

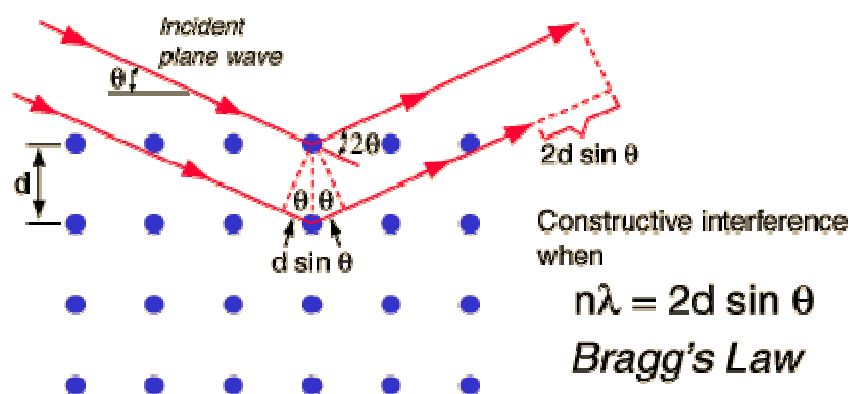


Figure 7. X-Ray scattering

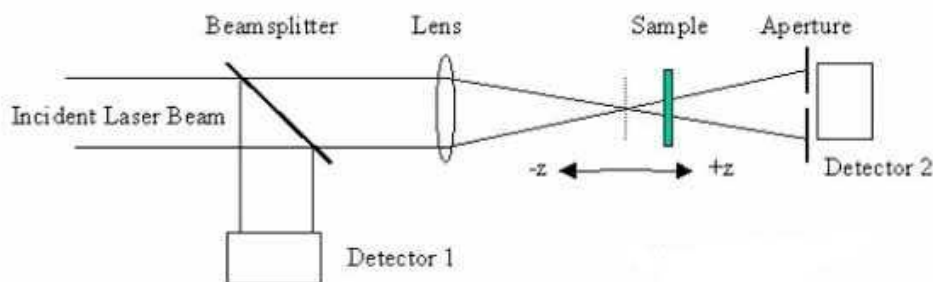
XRD experiments are used for the identification of unknown crystalline substances, since XRD patterns are unique for each substance and thus comprises its “fingerprint”. The technique was used in this study for the identification of the CdS quantum dots formed in the material. The samples were prepared by spin coating a glass slide with the cadmium containing hybrid material. The samples were polymerized under a UV lamp (maximum wavelength 365 nm) overnight and then were immersed in an aqueous Na_2S solution leading to the quantum dot formation.

The films were placed in a holder, and then illuminated with x-rays of a fixed wavelength (1.54 Å). The intensity of the reflected radiation was recorded using a goniometer. These data were then analyzed for the identification of the crystal structure and the calculation of the particle size using the Debye-Scherrer formula.

2.4.5 Z-Scan

As described in section 1.3.2, self-focusing or self-defocusing processes are derived from the combined action of an intensity dependent refractive index and the spatial variation of the laser intensity in which the beam is more intense in the center than at the edges. The self-focusing effect has also been used for the measurement of optical nonlinearity. There are numerous techniques for the measurement of nonlinear refraction in materials. These include, non-linear interferometry, degenerate four-wave mixing, nearly degenerate three-wave mixing, ellipse rotation and beam distortion measurements. The first three methods, interferometry and wave mixing are potentially sensitive techniques, but require a complex experimental apparatus. Beam-distortion measurements, on the other hand, require precise beam scans followed by detailed wave-propagation analysis. Sheik-bahae *et al.* (1989) used a z-scan method based on self-focusing to measure the sign as well as the magnitude of $\chi^{(3)}$. In this method a single beam is used for measuring refractive index nonlinearities, which offers simplicity as well as high sensitivity [38]. The same technique was used in this study for the measurement of the nonlinear index of refraction, n_2 in the QD doped hybrid material.

The Z-scan experimental set up is shown in figure 8. Using this set up the transmittance of a nonlinear medium is measured through a finite aperture in the far field as a function of the sample position z measured with respect to the focal plane.



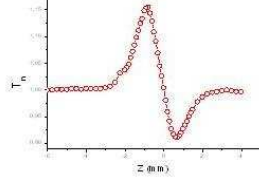


Figure 8. The Z-scan method

As an example, assume a material with a negative nonlinear refractive index and a thickness smaller than the diffraction length of the focused beam (thin medium). This can be regarded as a thin lens of variable focal length. Starting the scan from a distance far away from the focus (negative z), the beam irradiance is low and negligible nonlinear refraction occurs, hence, the transmittance ($D2/D1$, see figure 8) remains relatively constant. As the sample is brought closer to the focus, the beam irradiance increases, leading to self-lensing in the sample. A negative self-lensing prior to focus will tend to collimate the beam, causing a beam narrowing at the aperture which results in an increase in the measured transmittance. As the scan in z continues and the sample passes the focal plane to the right (positive z), the same self defocusing increases the beam divergence, leading to beam broadening at the aperture, and thus a decrease in transmittance. This suggests that there is a null as the sample crosses the focal plane. This is analogous to placing a thin lens at or near the focus, resulting in a minimal change of the far field pattern of the beam. The z-scan is completed as the sample is moved away from focus (positive z) such that the transmittance becomes linear since the irradiance is again low [39].

A prefocal transmittance maximum (peak) followed by a postfocal transmittance minimum (valley) is, therefore, the z-scan signature of a negative refractive nonlinearity. Positive nonlinear refraction, following the same analogy, gives rise to an opposite valley-peak configuration.

In a Z-scan experiment the laser beam must be Gaussian (TEM_{00}). Then the intensity profile of the beam will have a Gaussian distribution

$$I(r, t) = I_0 \frac{w_0^2}{w(z)^2} e^{\frac{-2r^2}{w(z)^2}} \quad (2.1)$$

where, $w(z)^2 = w_0^2 \left(1 + \frac{z^2}{z_0^2}\right)$, is the beam radius, $z_0 = k \frac{w_0^2}{2}$, is the diffraction length of the beam, $r = \sqrt{x^2 + y^2}$ is the distance of the point to the center of the beam, $k = \frac{2\pi}{\lambda}$

the wave vector and λ is the laser wavelength. There is a phase change due to nonlinear refractive index. This phase shift which follows the radial variation of the incident irradiance at a given position of the sample z , is given by

$$\Delta\varphi(r, z, t) = \frac{\Delta\varphi_o(t)}{1 + \frac{z^2}{z_o^2}} \exp\left[-\frac{2r^2}{w(z)^2}\right] \quad (2.2)$$

with

$$\Delta\varphi_o(t) = \frac{2\pi}{\lambda} \Delta n_o(t) \frac{1 - e^{-\alpha L}}{\alpha} \quad (2.3)$$

where, L is the sample length, α the linear absorption coefficient and $\Delta n_o = n_2 I_o(t)$, with $I_o(t)$ being the on axis irradiance (i.e., $z = 0$). The phase change of the optical wave inside the medium is proportional to the refractive index. With some reasonable approximations (such as thin sample, small phase distortion), one can derive the normalized transmittance of the closed-aperture z-scan:

$$T(z, \Delta\varphi_o) \cong 1 - \frac{4\Delta\varphi_o x}{(x^2 + 9)(x^2 + 1)} \quad (2.4)$$

where, $x = \frac{z}{z_o}$

In the above figure describing the Z-scan, one must bear in mind that a purely refractive nonlinearity was considered assuming that no absorptive nonlinearities (such as multiphoton or saturation absorption) are present. Qualitatively, multiphoton absorption suppresses the peak and enhances the valley, while saturation produces the opposite effect. The sensitivity to nonlinear refraction is entirely due to the aperture, and removal of the aperture eliminates the effect. Nonlinear absorption coefficients can be extracted from such ‘‘open’’ aperture experiments. If this is the case, the nonlinear refraction can be also measured in the presence of a nonlinear absorption. This can be done by a simple division of the curves obtained from the two open and closed aperture Z-scans. This gives a curve that closely approximates what would be obtained with a closed aperture Z-scan on a material having the same Δn but with zero nonlinear absorption. This greatly simplifies determining Δn .

The experimental setup we have used for the Z-scan measurements is the same as that in figure 8. The laser beam for this experiment was produced by a Ti-Sapphire femtosecond laser centered at 800 nm wavelength with 200 fs pulse duration, which gives 1 mJ pulses with a 1 KHz repetition rate. The laser beam is focused along the Z-axis by a lens with focal length, $f = 10$ cm and the signal transmitted is recorded on an oscilloscope through a photodiode. An iris placed in front of the detector serves as the

aperture. The sample sits on a linear translation stage and moves along the z-path (from positive to negative values) using a Labview control program.

The ultra-fast pulse has two advantages in the n_2 measurement: a) high instantaneous power that allowed us to measure small n_2 , b) low pulse energy and short pulse duration that allowed us to rule out the thermal and molecule reorientation effects. Therefore, in our experiment, the electronic polarization is the major contribution to n_2 .

2.4.6 White light diffraction

It is known from solid state physics, that when electromagnetic radiation passes through a periodic arrange of atoms or molecules, Bragg's law is satisfied and the incident radiation is refracted at certain angles, depending on the crystalline lattice, and diffraction patterns appear. In order for this to be observed, the wavelength of the incident radiation must be of the order of the periodicity of the lattice. The same principle is valid for all magnitudes of periodicity.

As mentioned in section 1.4, photonic crystals are periodic structures with periodicity of the order of the wavelength of light, so such structures will produce diffraction patterns if electromagnetic radiation of several hundreds of nanometers, strikes their lattice [40].

Woodpile structures with periodicity varying from 900 nm to 500 nm were fabricated via two-photon polymerization. In order to ensure the high quality periodicity of the fabricated structures, diffraction patterns were taken using a white light source in normal incidence. The set up used for this experiment is shown in figure 9.

A Ti-Sapphire laser beam centered at a wavelength of 800 nm with pulse duration of 200 fs is tightly focused onto a cell containing distilled water producing a white light beam. The white light is collected by a lens and focused onto the sample, which is placed on top of a 3D translational stage. Diffraction patterns are projected onto a screen, placed behind the sample.

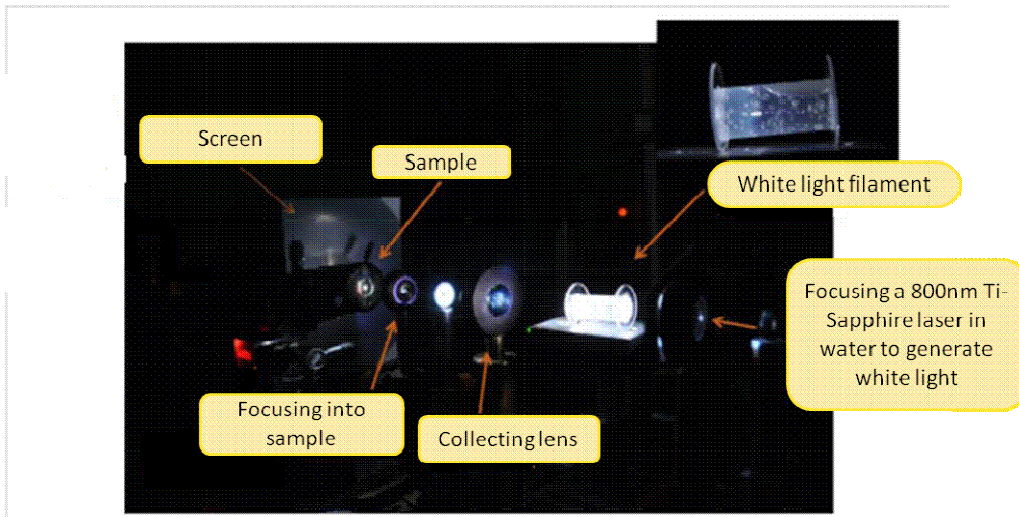


Figure 9. Experimental set up used for diffraction pattern imaging

2.4.7 Pump-probe

Pump-probe measurements can be used to obtain information on ultrafast phenomena [41]. The general principle is the following. A sample is hit by some pump pulse, which generates some kind of excitation (or other modification) in the sample. After an adjustable time delay (controlled with an optical delay line) a probe pulse hits the sample and its transmission or reflection is measured. By monitoring the probe signal as a function of the time delay, it is possible to obtain information on the decay of the generated excitation, or on other processes initiated by the pump pulses.

The pump-probe technique was used to measure the optical switching effect of a 3D photonic crystal. The set up used is depicted in figure 10.

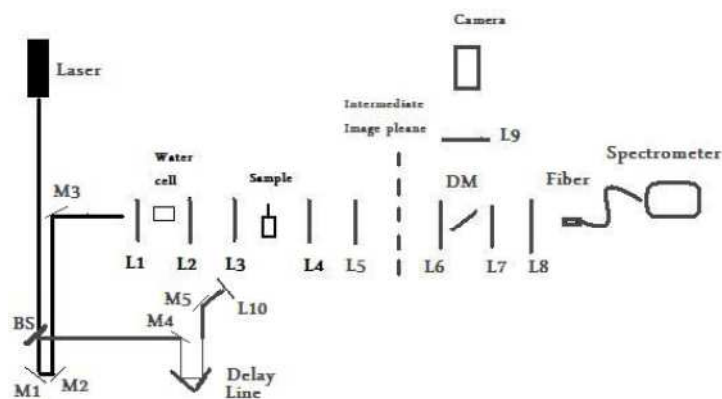


Figure 10. The pump-probe set up

A Ti-sapphire laser beam centered at 800 nm was used to generate the white continuum and is halved at the exit of the amplifier. Thus, one part of it was used as the pump beam for the experiment and the other half as the probe white light. A beam splitter (BS) is used to split the beam into two arms. The probe beam is directed through the mirrors M1, M2 to its initial path, whereas the pump beam through mirrors M4, M5 is directed and focused by lens L10 ($f = 20\text{cm}$) onto the sample. Lenses L3 and L10 ensure the spatial overlapping of the pump and probe beam at focus, whereas, a delay line in between mirrors M4, M5 serves for their temporal coherence. The latter is checked by observing the sum frequency generation (second harmonic generation) in a BBO crystal. The focal length of the L10 lens is chosen to be higher than that of the probe thus, the size of pump beam spot on the sample was much larger than that of the probe beam as to ensure better spatial overlap at focus. Therefore, when carrying out the experiment, initially the time zero for the pump and probe beam is defined by using the BBO crystal. In sequence, the sample is placed on top of the holder. Then, under white light continuum illumination, the diffraction pattern of the sample is observed (ensuring that the sample is well orientated and positioned near focus).

CHAPTER 3 RESULTS & DISCUSSION

3.1 Cadmium composite material

The cadmium containing composite material was used for the in situ synthesis of CdS quantum dots into the volume of 3-Dimensional photonic crystals (woodpile geometry) as well as into thin films. The 3D microstructures were characterized by Scanning Electron Microscopy and EDS before and after the formation of the nanoparticles. Thin films were used for the characterization of the semiconducting nanoparticles, by UV-Vis spectroscopy, fluorescence spectroscopy and X-Ray diffraction.

For the characterization of the CdS nanoparticles, by UV-Vis and fluorescence spectroscopy and XRD, thin films were prepared before and after the formation of the nanoparticles. As seen in figure 1, the films before the formation of the CdS quantum dots are slightly yellow. BIS gives this color when dissolved in the solution. After immersion in the Na₂S solution and rinsing, a remarkable difference in the color of the films is observed. The films obtain a deep yellow color, characteristic of the CdS nanoparticles.

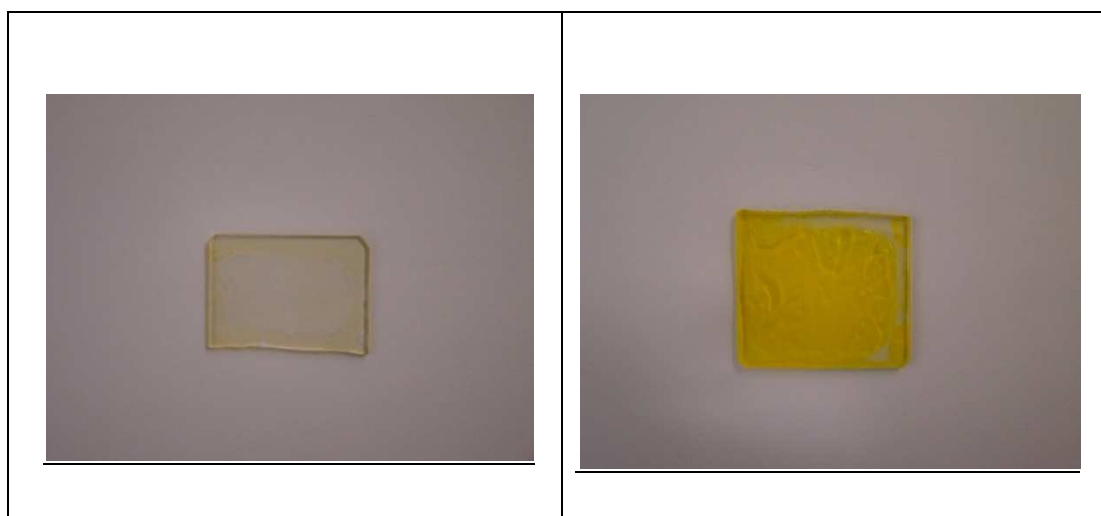


Figure 1. Thin films on glass slides before (left) and after (right) the formation of the nanoparticles

3.1.1 UV-Vis spectroscopy

The UV –Vis absorption spectra of the CdS nanocomposites were recorded by Perkin Elmer, Lambda 650 UV-Vis spectrophotometer. The absorption spectra were obtained from thin films, prepared by spin coating (Semiconductor Production Systems, Spin 150) onto glass substrates. Four samples were prepared. The first was a glass substrate, which was used as a reference. The second film was prepared from the zirconium 8:2 (MAPTMS to zirconium molar ratio), 1:1 (zirconium to MAA molar

ratio) composite material. The third was from the zirconium-cadmium composite material before the quantum dot formation and the fourth film was the zirconium-cadmium composite material, after treatment with Na₂S solution, in which the CdS quantum dots were formed.

Figure 2, shows the absorption spectra of the above described films.

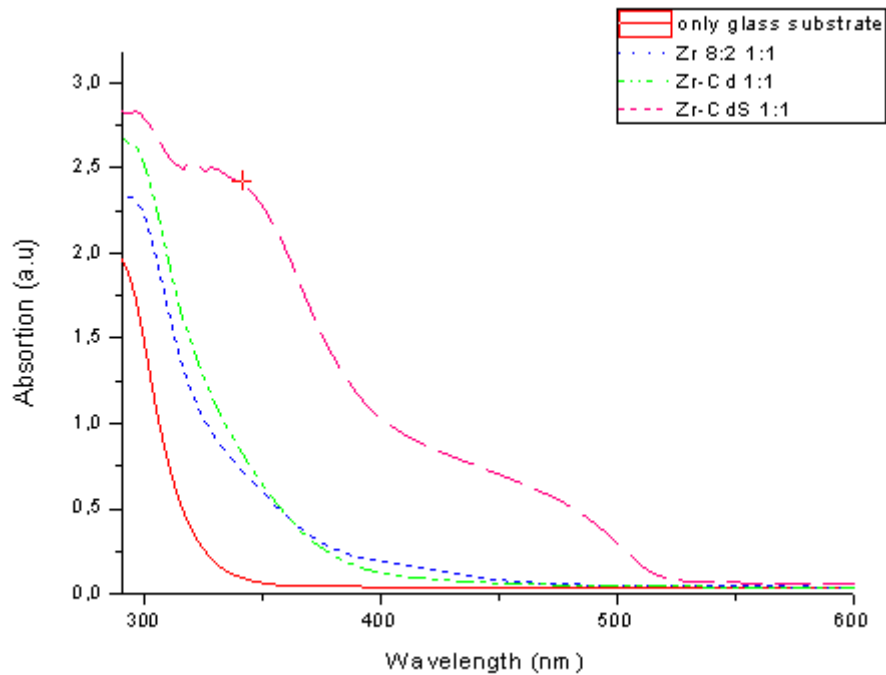


Figure 2. Absorption spectra of glass (red), zirconium (blue), zirconium-cadmium (green) and zirconium-CdS (magenta) composite thin films

As shown in figure 2, the glass substrate demonstrates zero absorbance above 350 nm. The absorbance of the zirconium composite films is negligibly different from the zirconium-cadmium one and is low above 350 nm. This allows us to make the assumption that there is no significant change to the zirconium composite material after the addition of cadmium methacrylate. On the other hand, an increase in absorption above 350 nm, after the formation of the CdS nanoparticles is readily apparent. It is also easily observed that the absorption spectrum of the CdS nanoparticle containing film shows a series of overlapping peaks, that become more intense at shorter wavelengths. Such an absorption spectrum is characteristic for quantum dots. Each peak corresponds to an energy transition between electron-hole (exciton) energy levels. The absorption onset, referred to the first exciton peak,

appears at about 340 nm, which corresponds to the near-UV region of the electromagnetic radiation.

Usually, quantum dots absorb in the UV range and emit radiation, fluoresce, in the visible region.

3.1.2 Photoluminescence spectroscopy

For the photoluminescence experiments, three samples were prepared. The first was a thin film of the zirconium 8:2, 1:1 composite, the second a thin film of the zirconium-cadmium composite material and the third a thin film of the zirconium-cadmium hybrid after treatment with the Na_2S solution, leading to the formation of the CdS nanoparticles. For all samples, silicon substrates were used. Figure 3, shows the fluorescence spectra of the above samples.

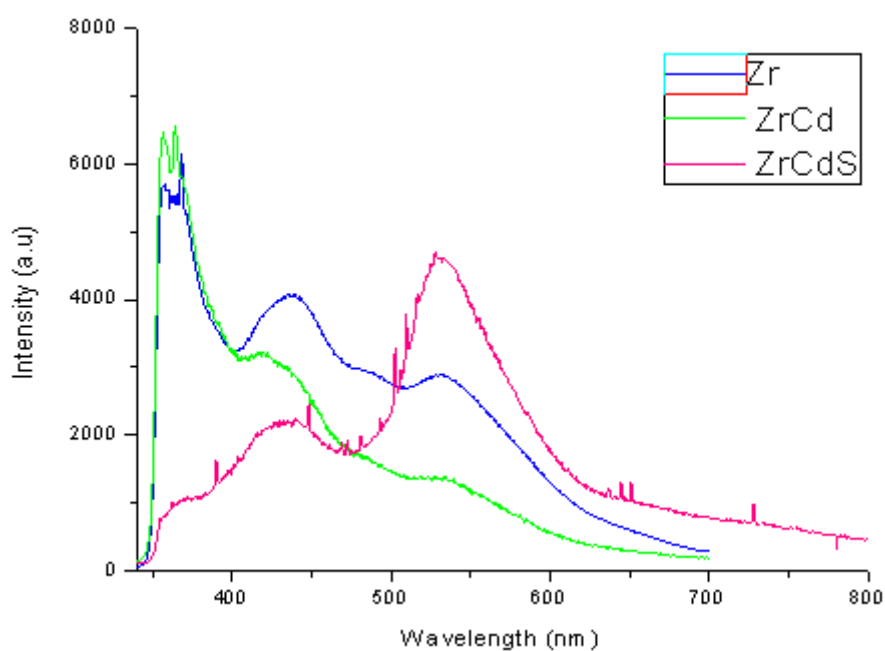


Figure 3. Fluorescence spectra of the zirconium (blue), zirconium-cadmium (green) and zirconium-CdS (magenta) composite thin films.

The blue line corresponds to the fluorescence spectra of the zirconium 8:2, 1:1 film. The green line corresponds to the zirconium-cadmium 8:2, 1:1 material before the formation of the CdS nanoparticles and the magenta line corresponds to the zirconium-cadmium film after the formation of the CdS quantum dots. The fluorescence of the zirconium composite material is attributed to the photoinitiator used. After the addition of cadmium methacrylate a reduction in the fluorescent intensity of the sample is observed, and the peaks at 440 nm and 530 nm diminish.

This was attributed to the reduction of the concentration of the photoinitiator in the composite solution, after the addition of cadmium methacrylate. Finally, after the formation of the CdS nanoparticles a very intense peak at 530 nm appears. This peak is attributed to the fluorescence of the nanoparticles, at the green region of the visible spectrum. The peak emission wavelength appears to be Gaussian (bell-shaped), characteristic for nanoparticles, and occurs at a longer wavelength than the absorption onset. This energy separation, referred to as the Stoke' shift, arises from the loss of vibrational energy of the excited molecule, due to collisions with other molecules. On the other hand the emission broadening of the peak, implies a broad size distribution for the nanoparticles or nanoparticle aggregation.

3.1.3 X-Ray Diffraction

Cadmium sulfide exists in nature as two different minerals, hexagonal greenockite for the bulk material and cubic hawleyite in nanomaterials. The XRD patterns of the CdS quantum dot containing thin films was obtained in order to access the crystallinity of the nanoparticles formed. Figure 4, shows the XRD diffraction pattern of the composite.

The XRD patterns of the CdS containing film, exhibits broad peaks centered at 2θ values of 26.5, 44 and 51.8° attributed to the (111), (220) and (311) planes, respectively of cubic CdS. It is of interest to note that a mixture of hexagonal and cubic phases is routinely observed for CdS nanoparticles. The reason for that being is that the two phases have similar energy and the transformation from one to another is most feasible. However, the particle size plays an important role in determining the crystal structure. By reduction of the size the crystal goes from the hexagonal to the cubic structure, for particle sizes below 5 nm [42], whereas above this size the material will comprise from a mixture of both phases.

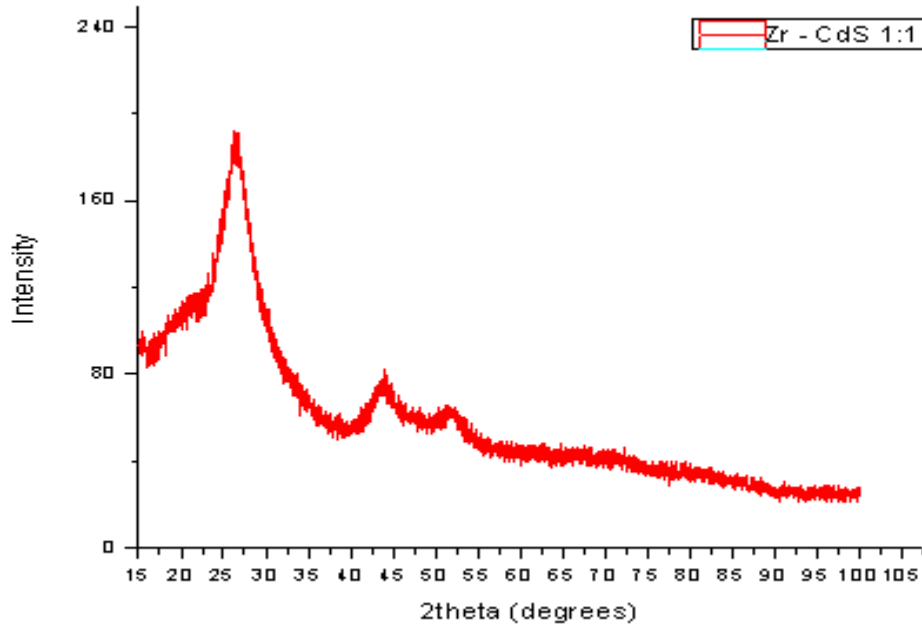


Figure 4. XRD pattern of the CdS containing films

The hexagonal structure has three distinct and closely located peaks at $2\theta = 24^\circ$, 26° and 29° , which are quite close to the intense peak of (111) of the cubic structure. In the present pattern the peak at 26.55° is symmetric and the (103) peak at 48° of the hexagonal phase is absent. This shows that the nanoparticles prepared in the current work exhibit cubic phase due to their small size.

The size of the nanoparticles was calculated using the Debye-Scherrer's formula:

$$D = 0,89 \lambda / B \cos(\theta)$$

where, D is the particle diameter, λ is the X-ray wavelength, B is the full width at half maximum of the integral breadth and θ is the Bragg angle. The average crystal size was estimated to be about 1.5 nm.

3.1.4 Scanning Electron Microscopy & EDS

The cadmium containing composite material was used for the fabrication of 3D microstructures. The CdS quantum dots were synthesized in the volume of these structures upon treatment with Na_2S . Elemental analysis was performed on the structures, before and after the formation of the quantum dots, using the EDS technique. The SEM pictures as well as the EDS spectra are shown below.

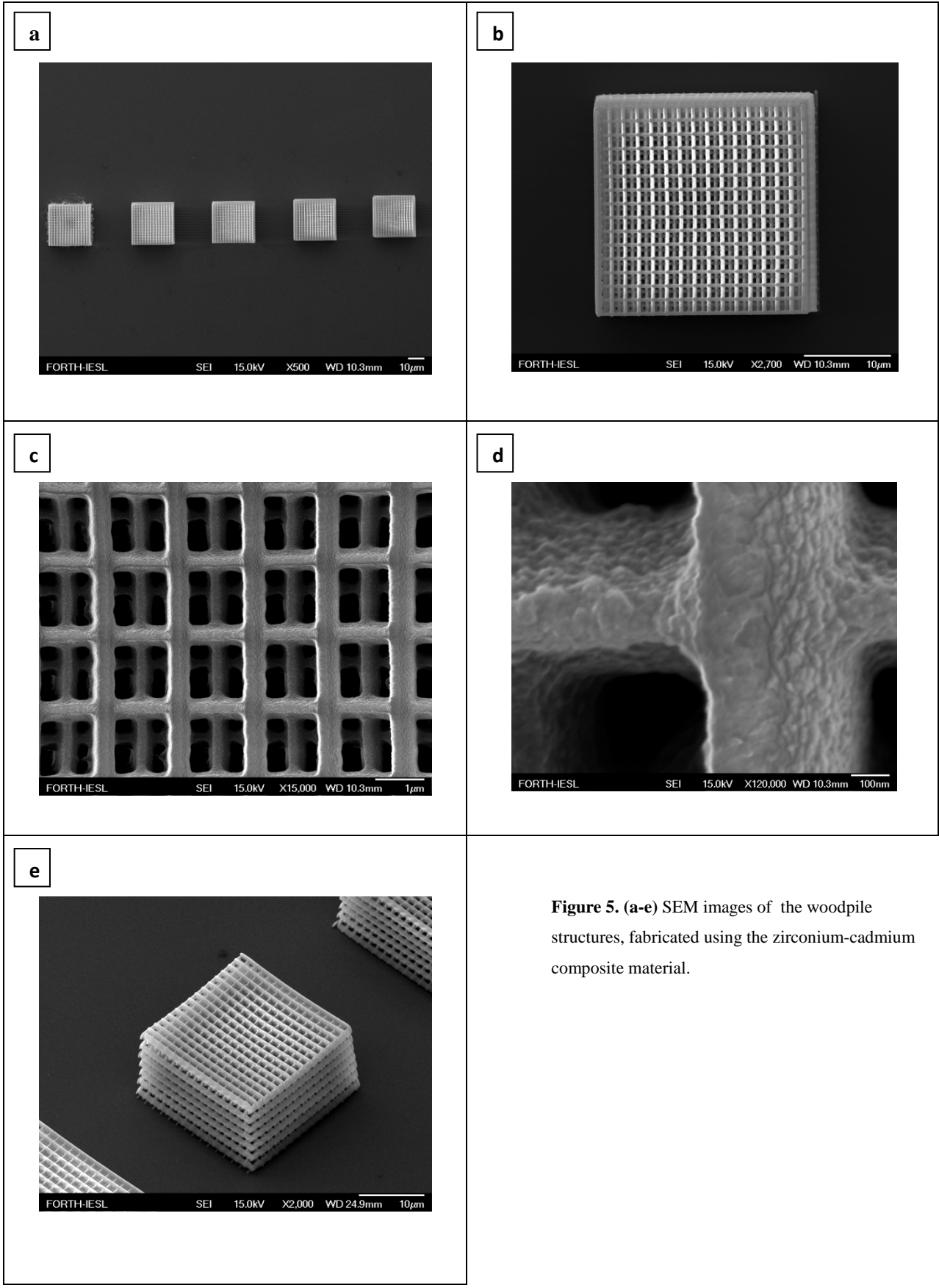


Figure 5. (a-e) SEM images of the woodpile structures, fabricated using the zirconium-cadmium composite material.

Figure 5, shows the woodpile structures before the formation of the nanoparticles. The structures demonstrate no shrinkage and high spatial resolution is achieved. The EDS spectra, obtained from these structures are shown in figure 6.

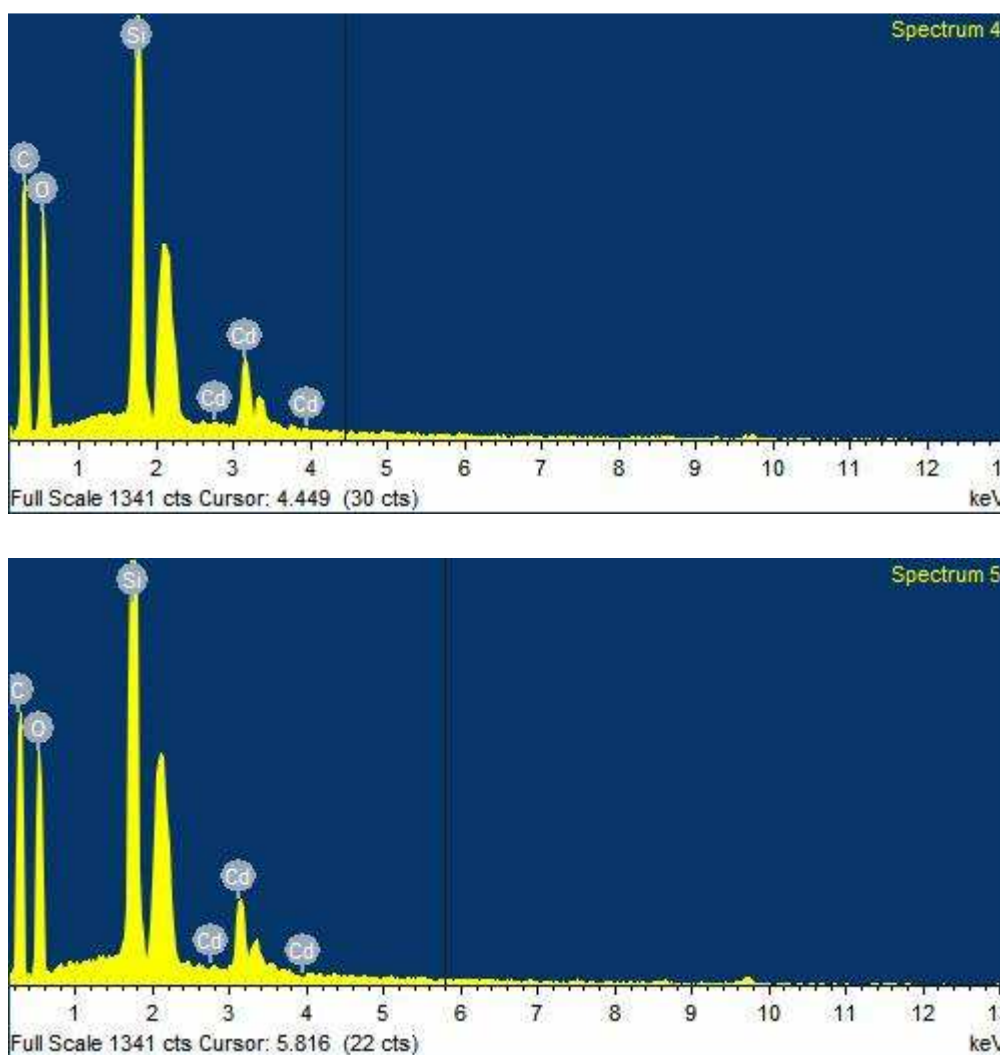


Figure 6. EDS spectra obtained from the structures of the zirconium-cadmium composite material. Spectrum 4 corresponds to image 5(c) whereas spectrum 5 corresponds to image 5(d)

Elemental analysis shows the presence of cadmium, in the material. The other elements that appear, are due to the organic monomers (carbon) and the inorganic network (oxygen, silicon).

Next, the SEM images of the structures after treatment with Na_2S are shown in figure 7.

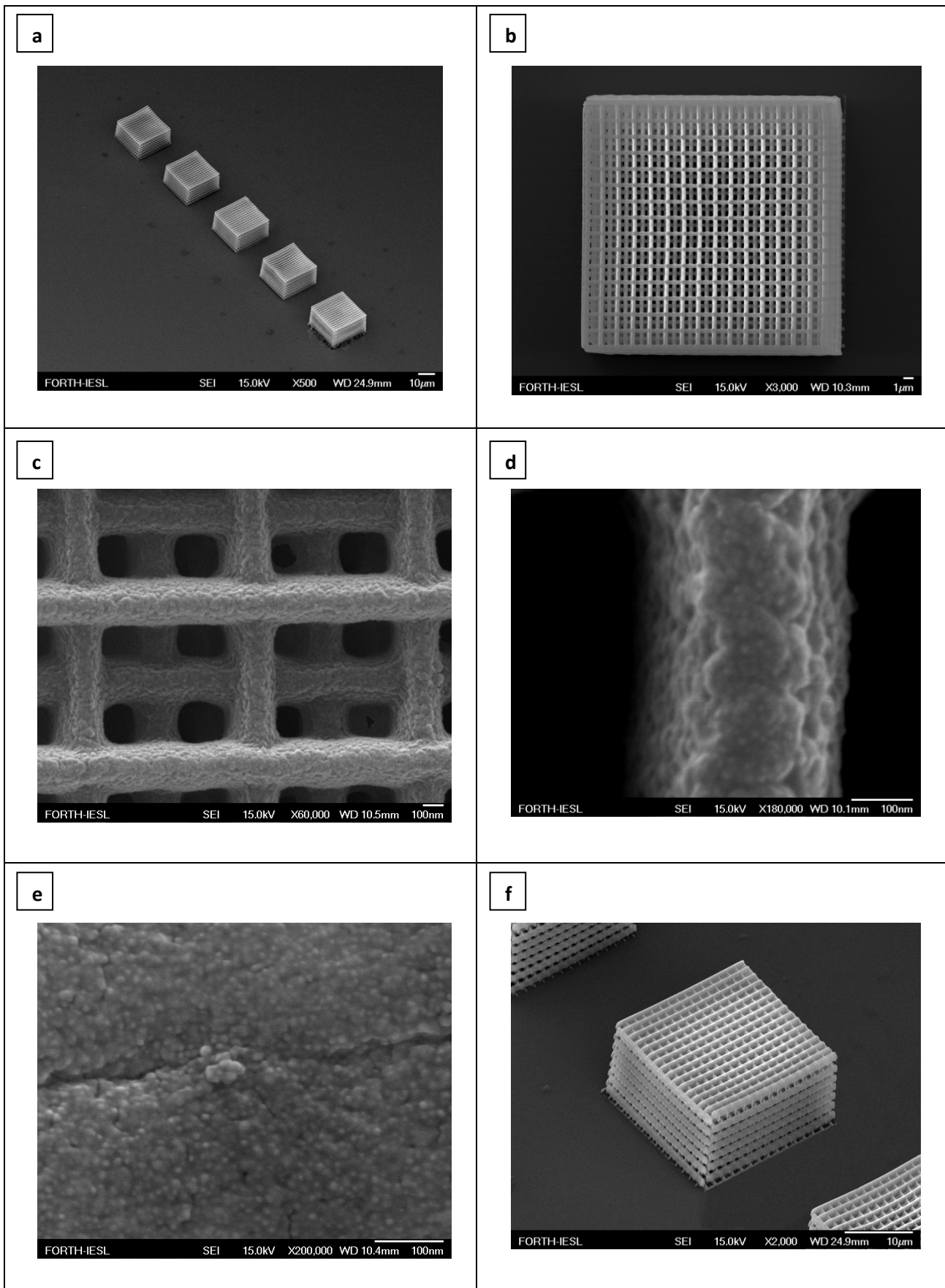


Figure 7. SEM of the woodpile structures, fabricated using the zirconium-cadmium composite material after treatment with Na_2S

As observed from pictures 7(a), (b), (c) and (f), treatment with sodium sulfide does not affect the shape of the structures. The EDS spectra of these structures are shown in figure 8.

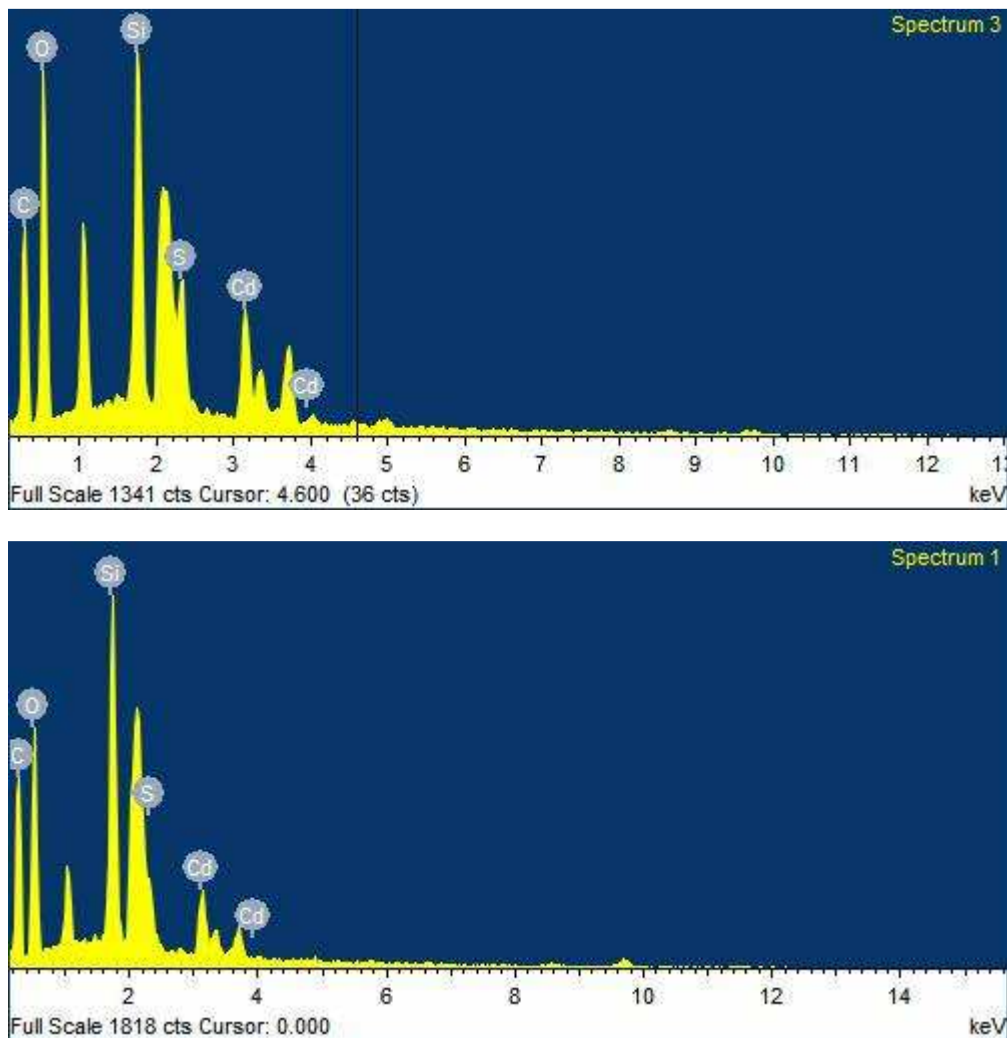


Figure 8. EDS spectra obtained for the structures of the zirconium-cadmium composite material after treatment with sodium sulfide. Spectrum 3 corresponds to image 7 (c) whereas spectrum 4 corresponds to image 7 (d)

The sulfur element appears in the spectra, and thus verifies the formation of the cadmium sulfide quantum dots.

3.1.5 Z-Scan

As mentioned in Chapter 1, quantum dots exhibit an intensity dependent refractive index or in other words they exhibit third order optical non-linearity. The z-scan technique (section 2.4.5) was used in order to measure the optical non-linearity of the CdS quantum dot containing film. The experimental setup used, is shown in figure 8, chapter 2.

The samples for the z-scan measurements were thin polymerized films of the cadmium-zirconium-DMAEMA composite material, after the formation of the CdS quantum dots. For the validation of the system, toluene and chlorobenzene were used, which are solvents that also exhibit third order optical non-linearity. The curves obtained are shown below.

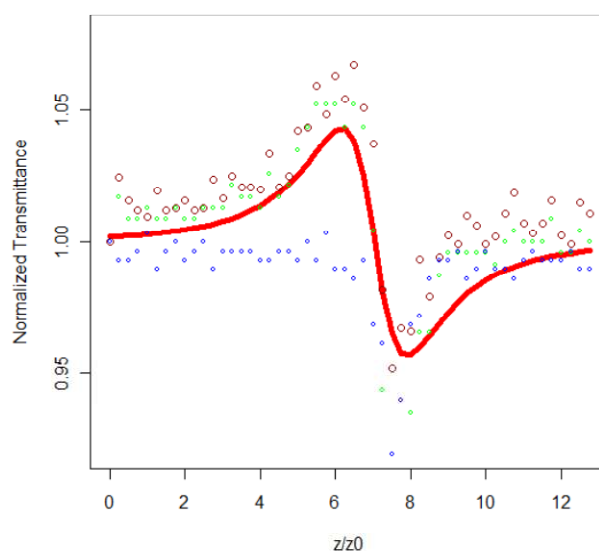


Figure 9. Z-scan curve for toluene

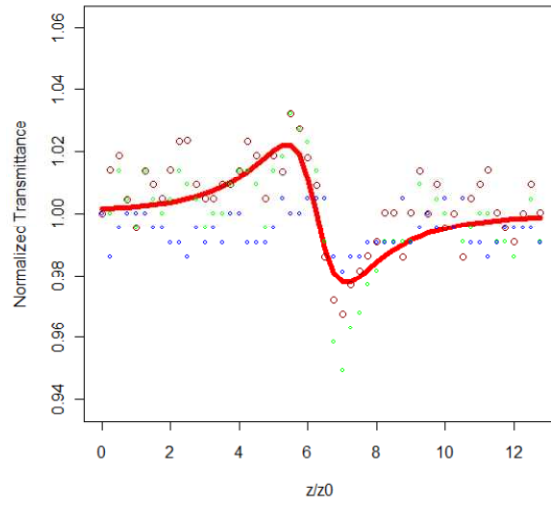


Figure 10. Z-scan curve for chlorobenzene

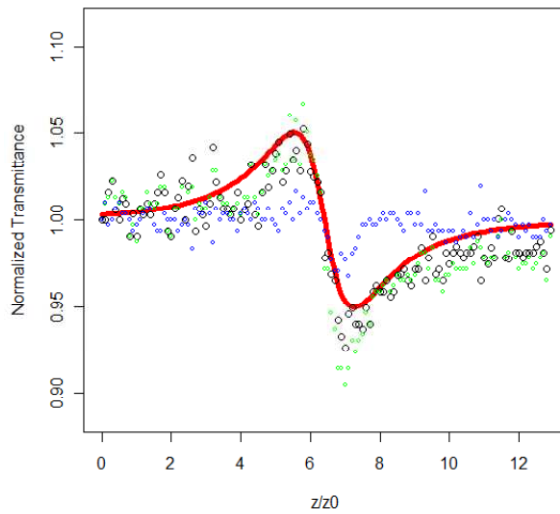


Figure 11. Z-scan curve for the CdS-zirconium-DMAEMA composite film

The measured close aperture z-scan trace is presented by a green dotted line, whereas the open aperture trace is marked with a blue dotted line. The net effect traced by the red line is fitted to equation (2.4) from where we can extract the nonlinear phase shift and the ratio $\frac{z}{z_0}$.

The z-scan curve of the CdS-zirconium-DMAEMA composite film exhibits the characteristic pick-valley appearance, which indicates the optical nonlinearity of the material. In particular, a positive nonlinearity is observed, since the peak-then-valley sequence was recorded as the sample translated towards the focusing lens. It should be mentioned that the open-aperture Z-scan trace at the same excitation intensity revealed negligible two-photon absorption and confirms that the observed third order nonlinearity is a result of the non-linear refraction.

3.2 3D structuring and characterization

3.2.1 High resolution 3D photonic crystals

The resolution of stereolithography depends on the size of the focal spot and is limited by diffraction, thus the minimum feature size cannot be smaller than half of the applied laser wavelength. Since TPA is nonlinear and displays threshold behaviour, structural resolution beyond the diffraction limit can be realized. Structures with feature size down to 100 nm can be fabricated, which is almost an order of magnitude smaller than the laser wavelength (800 nm). A voxel (volume pixel), which has the shape of an ellipsoid, can be seen as a basic structural unit (building block) polymerized in the focal volume by irradiation of the photosensitive material with the laser. Intensity threshold for polymerization is defined as the minimum laser radiation intensity required for the initiation of the polymerization process leading to an irreversible change in the material. 2PP is an accumulative process, which might result from the absorption of a number of pulses, and not necessarily of a single laser pulse. Finally, the size of the single voxel depends on the irradiation dose. Figure 12 illustrates the structural resolution as a function of the light intensity. Since only the area of the laser focus volume, where the intensity exceeds the polymerization threshold, will contribute to the 2PP process, the resolution can be tuned by adjusting laser power to be just above the polymerization threshold [43].

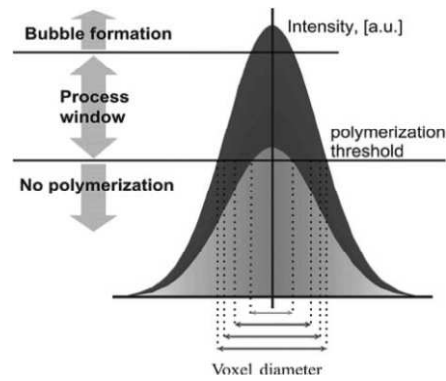


Figure 12. Structural resolution in 2PP

Although, working with power near the polymerization threshold can improve the resolution sufficiently, sometimes this is not enough. Great difficulties arise, as the period of the photonic crystals moves towards the short wavelengths (infrared and visible) that are the most important for lasers and optical communications. To give an example, suppose that one wishes to fabricate a woodpile structure with interlayer rod distance of $d = 500\text{nm}$. This means that the unit cell height will be $a = \sqrt{2} d = 707\text{nm}$ leading to an interlayer distance of $a/4 = 177\text{ nm}$ or the height of the rods to be less than 354nm ($h < c/4 \times 2$) for a partial interlayer overlapping to exist. This value is almost $1/3$ of the theoretical value of the $d = 1.2\text{ }\mu\text{m}$ given due to the laser wavelength and the imaging optics used.

In this work, photonic crystals with period down to 500 nm were fabricated exhibiting resolution up to 70 nm . In order for this to be achieved, near polymerization threshold laser power, chemical quenchers, appropriate solvents for developing and slow fabrication velocity were used [44]. Each one of those parameters plays an important role in fabricating high resolution woodpile structures with period reaching the visible wavelengths.

Besides low laser intensity, chemical quenching in combination with slow fabrication velocities, that allow the diffusion of the quencher in the scanned area, has shown to improve the multi-photon polymerization resolution dramatically. In the current work the quencher, 2-(dimethylamino)ethyl methacrylate, is also a photopolymerizable monomer and becomes part of the polymer backbone upon fabrication of the structures.

In our experiments, the addition of this quencher has caused major improvement in the spatial resolution of the written lattices. This means that the quencher not only has changed the level of the polymerization threshold, but it also affected the polymerization non-locally due to diffusion. The quencher used, DMAEMA, is not attached to the inorganic network, so, it can diffuse during the polymerization process. The time needed to write a single line of length $l_{line} = 30\mu m$ within the photonic crystal with scanning velocity $v = 20\mu m/s$ is $t_{line} = 1.5s$. As the diffusion coefficient of DMAEMA is $D_Q = 10^{-5} - 10^{-7} cm^2/s$, the estimated time of diffusion of it at the distance of $d_{period} = 400nm$ between the lines is $t_{diff1} = d_{period}^2 / D_Q = 1.6 \cdot 10^{-4} \div 1.6 \cdot 10^{-2} s$. That is, $t_{diff1} \ll t_{line}$, and therefore the quencher initial concentration recovers between line scans.

With N.A.=1.4 and $\lambda=800nm$ the beam radius is $r_{beam} \approx 180 nm$. Therefore, the irradiation time of a particular point is $t_{irr} = 2r_{beam}/v = 8 \cdot 10^{-2} s$. The estimated time of diffusion of DMAEMA through the irradiated domain is $t_{diff2} = r_{beam}^2 / D_Q = 3.2 \cdot 10^{-5} \div 3.2 \cdot 10^{-3} s$. That is, $t_{diff2} \ll t_{irr}$, and thus diffusion is important during single line scans as well.

To understand the effect of the quencher diffusion during the line scans, let us now consider a basic photopolymerization model. The evolution of the spatial distributions of the number densities of the quencher molecules (Q), free radicals (R) and free monomer molecules (M) can be modeled by the following equation set:

$$\frac{\partial R}{\partial t} = S(\vec{r}, t) - k_{tQ}QR, \quad (1)$$

$$\frac{\partial Q}{\partial t} = D_Q \Delta Q - k_{tQ}QR, \quad (2)$$

$$-\frac{\partial M}{\partial t} = k_p RM, \quad (3)$$

Free radicals are generated as a result of the absorption of laser light by the photoinitiator. For two-photon absorption, the source term is proportional to the square of the local field intensity, I , pulse duration t_p and pulse repetition rate R_p :

$S \propto I^2(\vec{r}, t) t_p R_p$. As a result of the quenching reaction, both the quencher and the radical are consumed with the reaction rate k_{tQ} . The diffusion coefficient of the quencher is D_Q , Δ is the Laplacian. The polymerization rate is given by Eq. (3) being proportional to the monomer number density, M , the radical number density and the propagation constant k_p . The conversion

$$p = \frac{M_0 - M}{M_0},$$

indicates the degree of polymerization (here, M_0 is the starting number density of the monomer).

Since the line scan is much slower than the diffusion of the quencher, i.e. $t_{diff} \ll t_{irr}$, one can consider long-lasting irradiation with constant in time point-like source. For simplicity, we take the spherically symmetric Gaussian source:

$$S = S_0 \exp(-r^2/2L^2) \quad (4)$$

Due to diffusion, the consumption of the quencher in the irradiated volume can be compensated by its transfer from non-irradiated domains. In such a balanced state the quencher number density distribution is maintained constant in time: $\partial Q/\partial t \equiv 0$. Examples of such calculated distributions are shown in Figure 13.

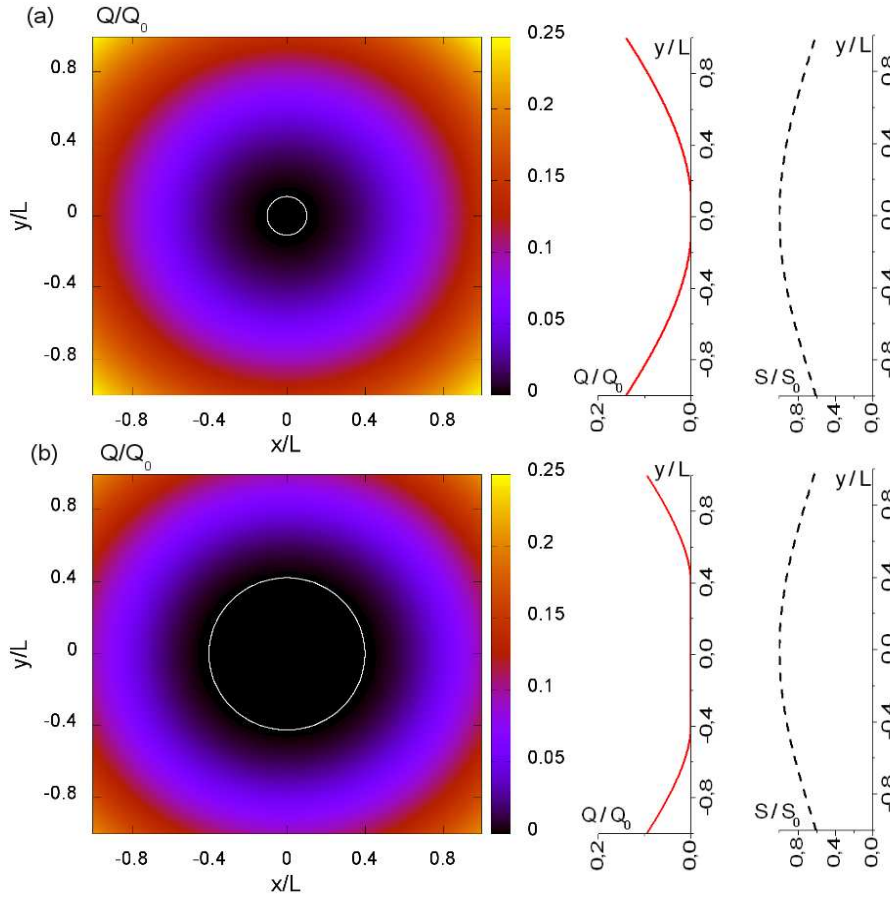


Figure 13. Calculated distributions of the quencher number density Q with respect to the initial quencher number density Q_0 (color maps and red line graphs). L is the width of the Gaussian radical source. Radii of the quencher-free domains (indicated with white circles) are $0.1 \cdot L$ (a) and $0.4 \cdot L$ (b). Ratio of the magnitudes of the laser beam intensity between cases (b) and (a) is $I_b/I_a \approx 1.038$. The distributions of the source of the radicals are plotted in black dashed line graphs.

It can be seen that there is no quencher in the central domain of the irradiated volume. The polymerization is inhibited only in the region that surrounds this domain. This effect is similar to the one reached in STED-DLW, however, in our case, one does not need any depletion beam.

By solving Eqs. (1-2) for the case of Gaussian radical source (4) one can analytically obtain the radius of the quencher-free domain:

$$r_1 = L \sqrt{2 \ln \left(\frac{S_0 L^2}{Q_0 D_Q} \right)}, \quad (5)$$

where Q_0 is initial quencher number density. It can be seen that the radius can be made arbitrarily small by tuning the laser beam intensity, since the radical source magnitude is $S \propto I^2(\vec{r}, t) t_p R_p$. The irradiation time, conversely, does not affect the size of the quencher-free domain. An increase in the irradiation time (or a decrease in the scan speed) only causes the increase in the polymerization degree (conversion) within the quencher-free domain. Contrary, in the threshold model (without quencher diffusion), the maximal polymerization degree of a nanofeature can be increased by applying higher irradiation dose either by increasing beam intensity or irradiation time (Fig.14). However, the higher dose inevitably results in increase of the size of the polymer feature. By employing the diffusion of the quencher, one can handle both the size and the maximal conversion of the polymer feature separately. Formation of sharp spatial distributions of the conversion is important for achieving high spatial resolution, high mechanical stability and stability against the fluctuations.

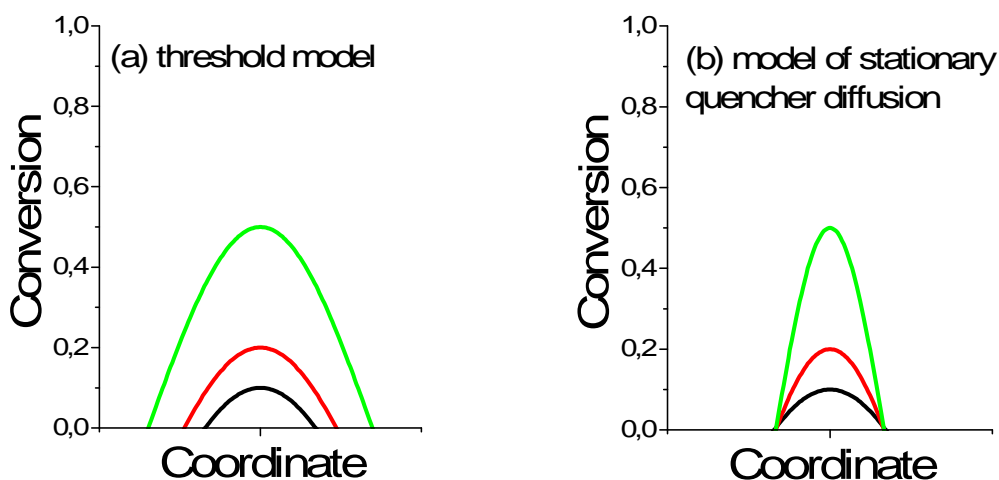


Figure 14. (a) Schematic representation of conversion profiles in threshold polymerization regime for different irradiation doses. (b) Schematic representation of conversion profiles in model of stationary quencher diffusion for different irradiation times and fixed irradiation intensity.

The last but not least parameter for achieving high resolution structures is developing. As the period of the structures moves down to 500 nm, the filling fraction increases. Thus, most of the solvents do not manage to penetrate inside the complex 3D

structures. However, if one manages to fabricate high resolution structures with high integrity, there is no point if it cannot be separated from the unpolymerized material.

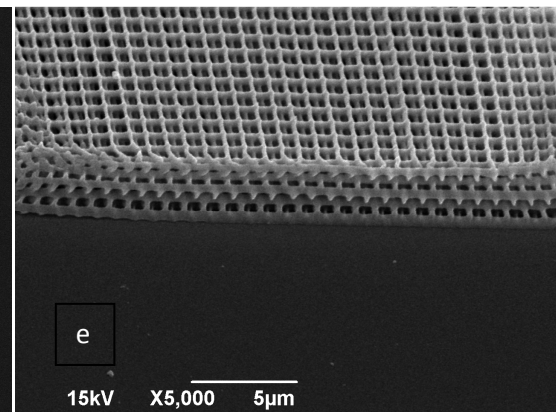
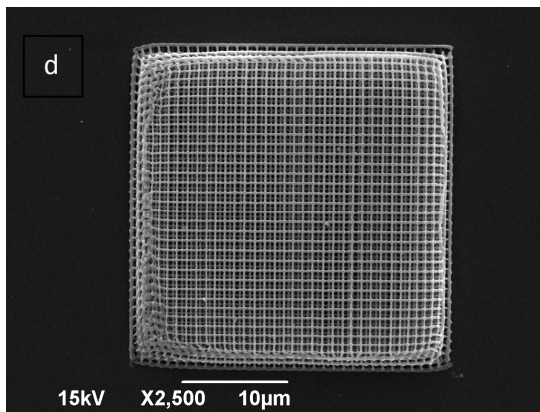
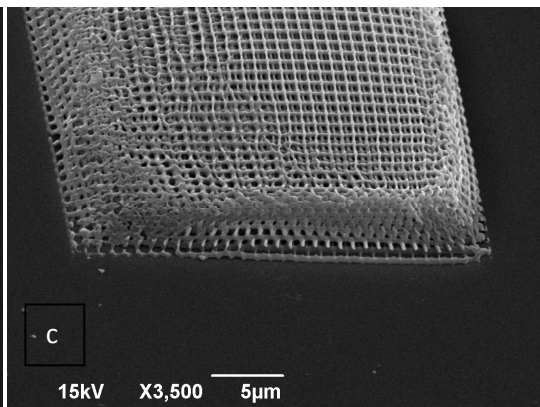
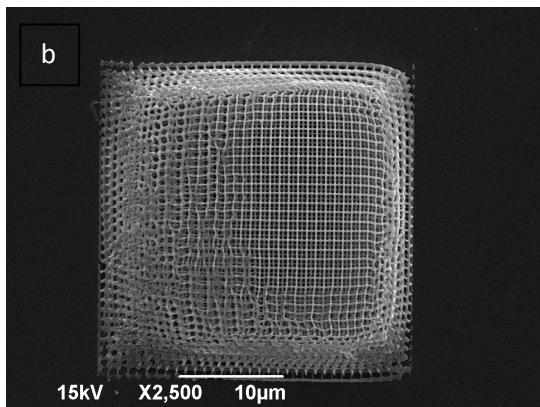
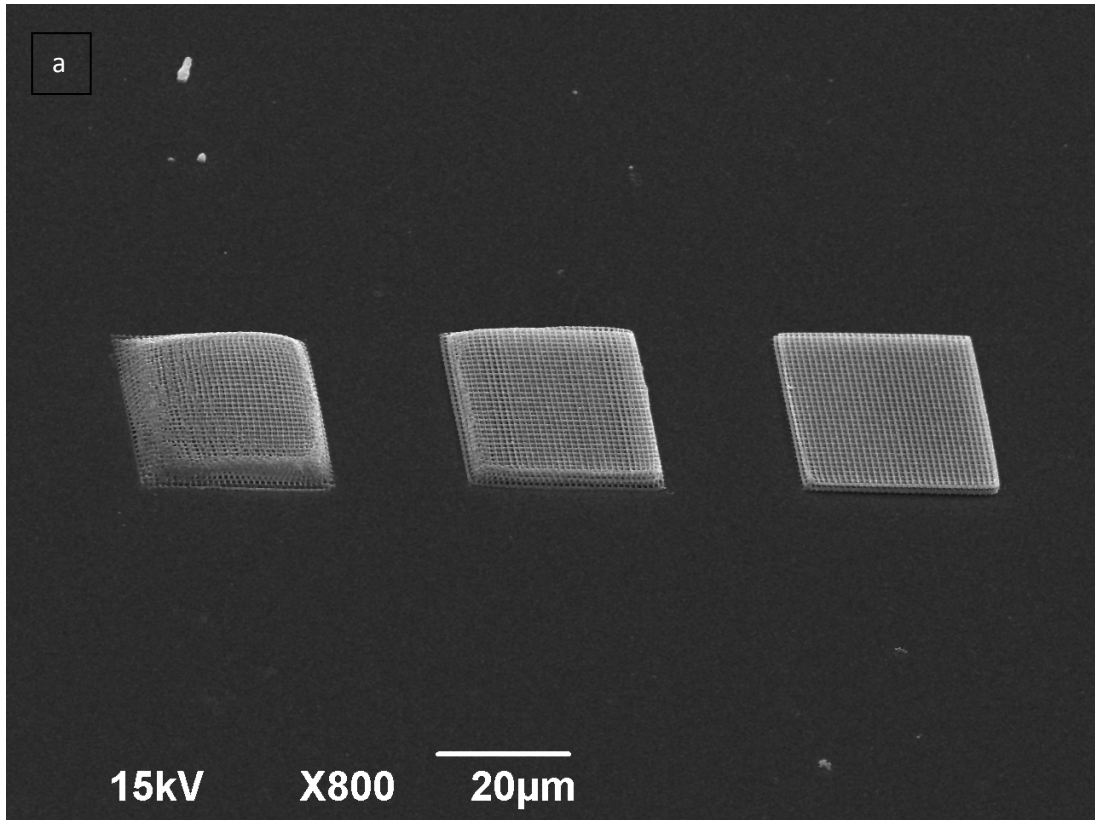
Thus, significant effort was put in order to find the correct combination of developing solvents. In fact, sequential development with 4-methyl-2-pentanone, 1-propanol and finally dimethyl sulfoxide has given the correct recipe. Any other combination of solvents or development in a different sequence, even using these three solvents did not have a successful result.

SEM pictures reveal that the combination of all the above mentioned parameters can result in 3D high resolution woodpile structures that exhibit high integrity and minimal distortion. Woodpile structures with period from 900 down to 500 nm were fabricated.

The material used for the fabrication of the woodpile structures is described in section 2.2. A range of energies, near the polymerization threshold, was investigated in order to find the optimum conditions for the fabrication of functional structures.

900 nm period woodpile structures

Figure 15 shows the SEM images of woodpile structures with interlayer periodicity of 900 nm. The range of energies tested ranged from 1.9 mW to 2.3 mW. Below 2.1 mW no structures survived, which indicated that this energy comprises the polymerization threshold.



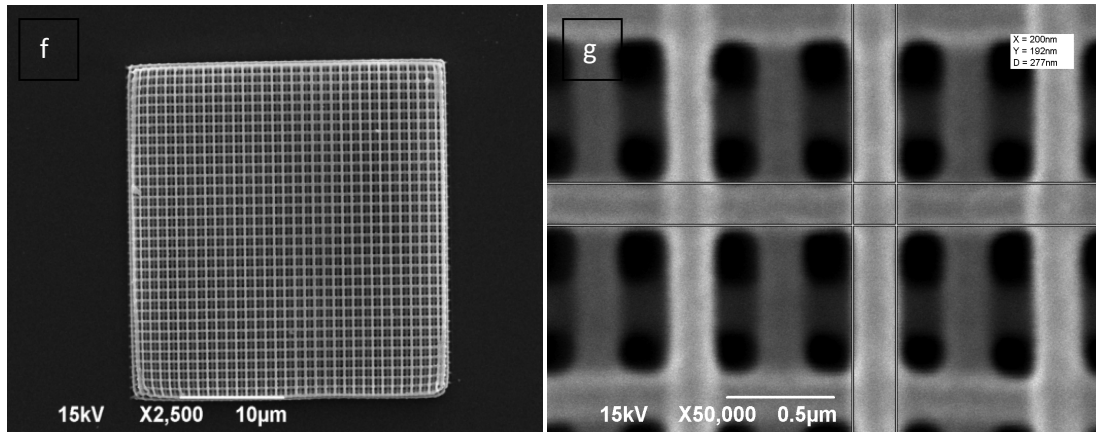
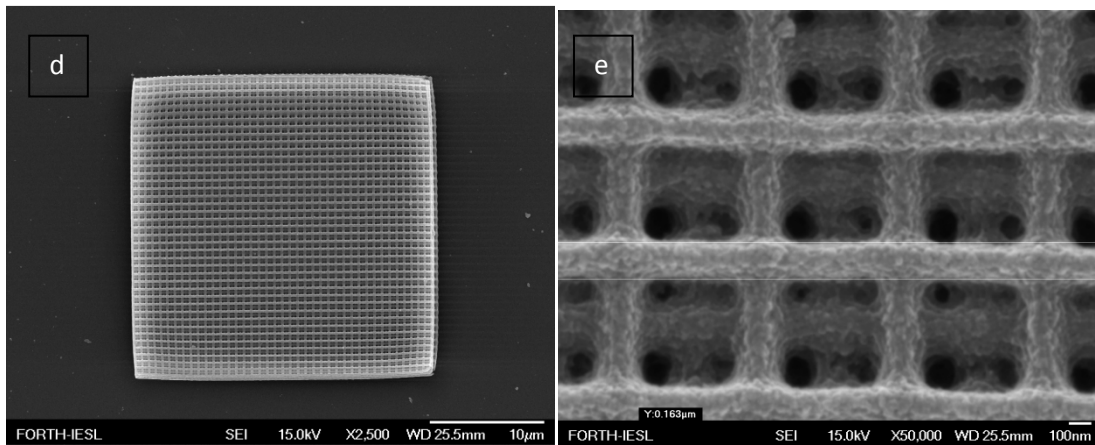
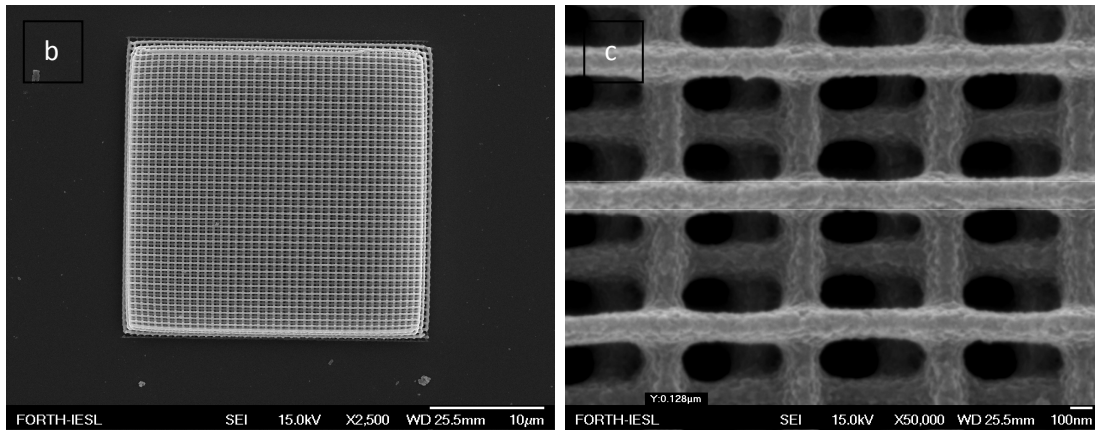
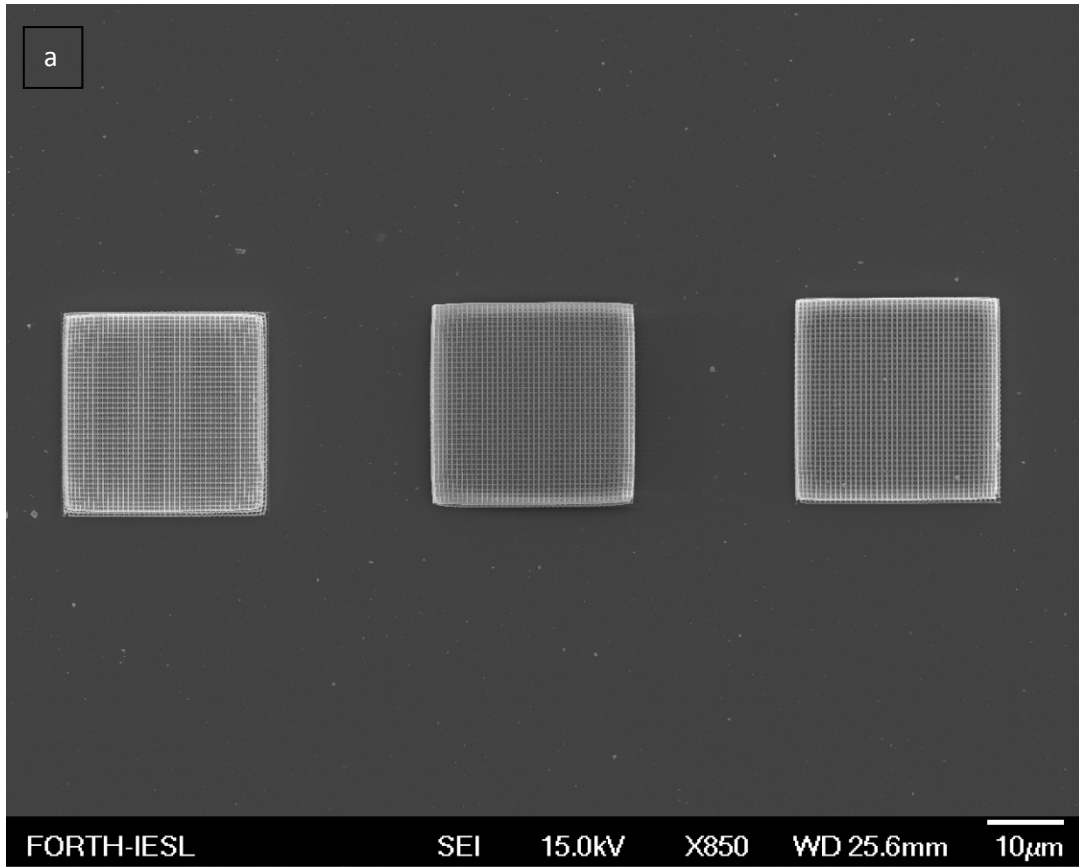


Figure 15. SEM images of 900 nm period woodpile structures. **a)** Overview of the woodpile structures. The fabrication energies are 2.1 mW- 2.3mW from left to right respectively **b-c)** closer view of the 2.1 mW structure **d-e)** closer view of the 2.2 mW structure **f-g)** closer view of the 2.3 mW woodpile structure.

Figures 15 (b) and (c) shows the 3D structure fabricated at the polymerization threshold. The structure exhibits high shrinkage and is partially deformed. Increasing the energy by 0.1 mW (figure 11 (d-e)) allowed a great improvement in the rigidity of the structure. Although some shrinkage exists, there are no obvious deformations. The optimum energy was found to be at 2.3 mW (figure 11 (f-g)) for which the woodpile structure exhibits minimal distortion and a resolution of 200 nm.

700 nm period woodpile structures

The energies investigated for the 700 nm interlayer periodicity woodpile structures varied from 1.8 mW – 2.2 mW (figure 16 (a)). The optimum energy was found to be 2.0 mW with a resolution of 128 nm (figures 16 (b-c)). Below 1.9 mW no structures survived, while at 2.1 and 2.2 mW (figure 16 (d-e) and 16 (f-g) respectively) the intralayer gaps started to polymerize and the resolution increases to approximately 165 nm.



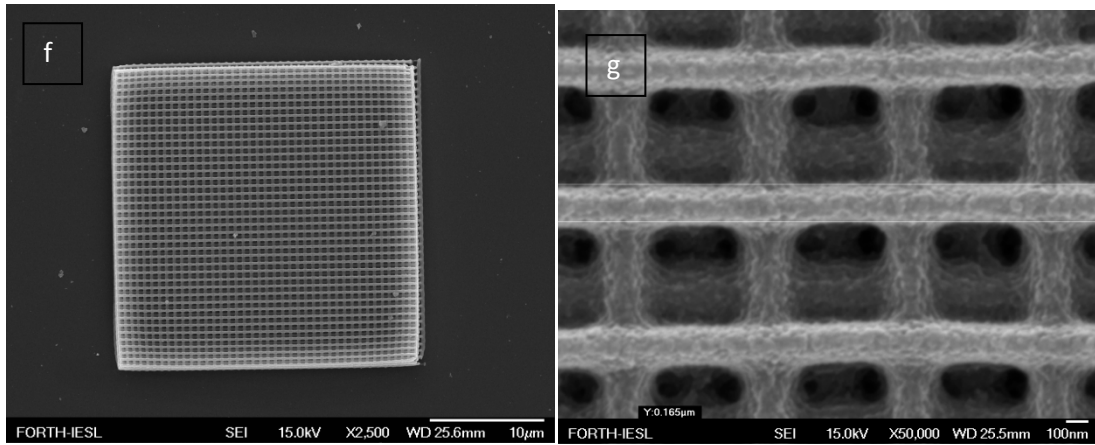
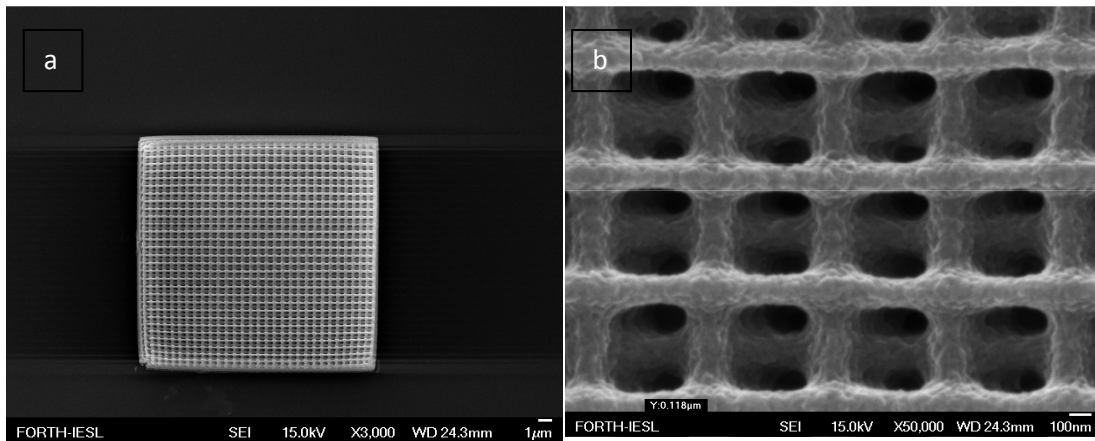


Figure 16. a) Overview of the 700 nm woodpile structures. The energies varied from 2.0 mW-2.2 mW from left to right respectively b-c) the woodpile structure fabricated using 2.0 mW energy d-e) the woodpile structure fabricated using 2.1 mW f-g) the woodpile structure using 2.2 mW

600 nm period woodpile structures

Figure 17 depicts the SEM images of woodpile structures with 600 nm interlayer periodicity. In order to find the conditions for the fabrication of the 600 nm period woodpile structures, again an energy test was carried out. The optimum energy was found to be at 1.9 mW (figure 17 (a-b)). Using energies below (figure 17 (c-d)) or above 1.9 mW (figure 17 (e-f)) gave structures that exhibited high deformation and shrinkage or structures that almost looked like solid cubes respectively.



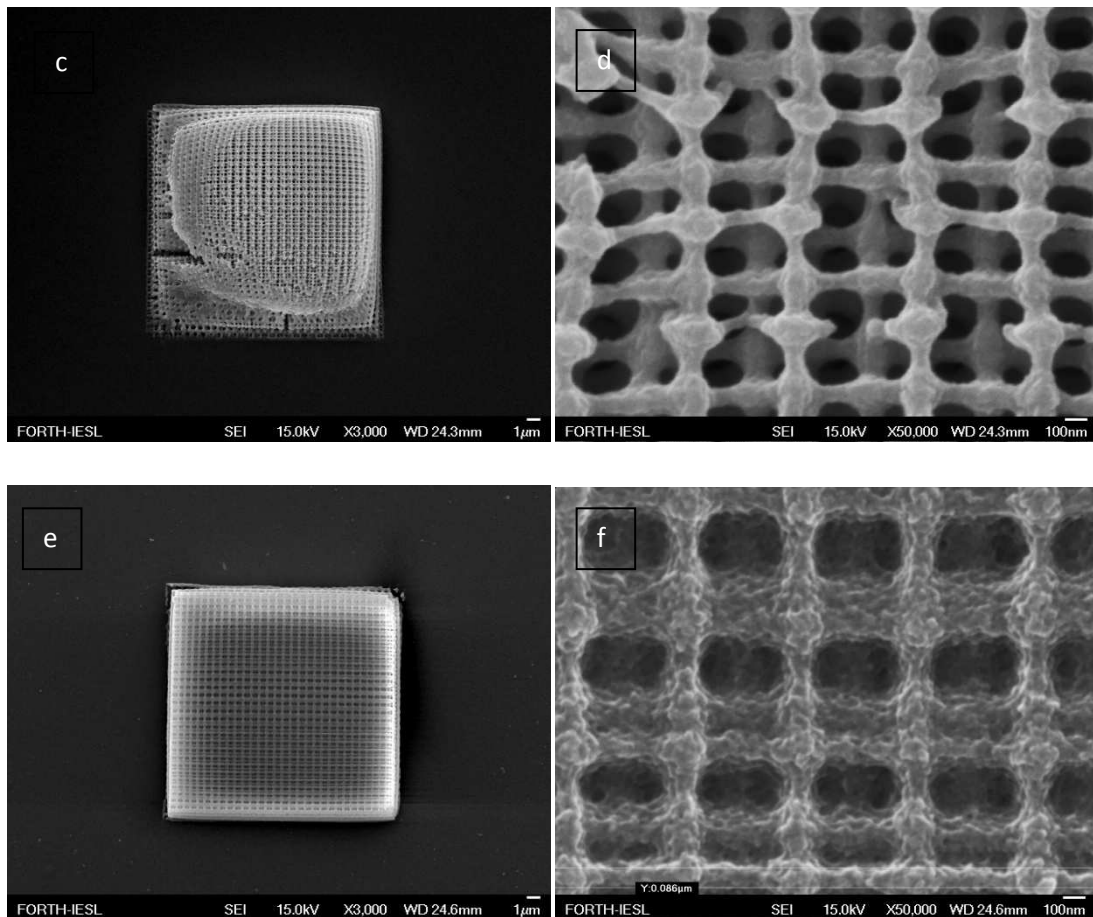


Figure 17. a-b) SEM images of 600 nm period woodpile structures fabricated using 1.9 mW energy c-d) the same structures using energy below 1.9 mW e-f) and the same structures fabricated using energy above 1.9 mW

500 nm period woodpile structures

The most challenging task of the current thesis was the fabrication of functional 3D woodpile photonic crystals with period of 500 nm and below which will exhibit stopgaps at and near the visible wavelengths. SEM images (figure 18) revealed the high quality woodpile structures with rod spacing of 500 nm. The structures exhibited high integrity and minimum shrinkage effects while their resolution reached 70 nm.

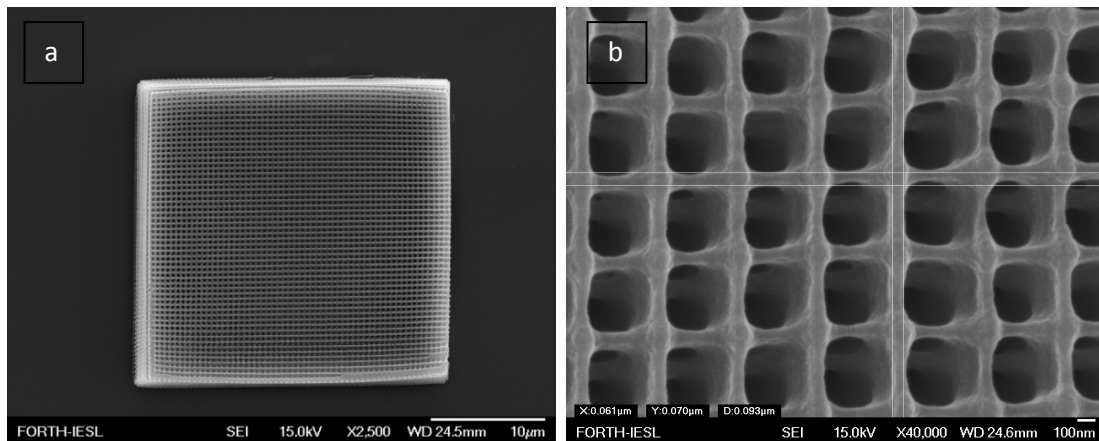


Figure 18. a) SEM image of the 500 nm period woodpile structure b) closer view of the same structure with a resolution of 70 nm

The energy used for the fabrication of the structures was 1.8 mW. In order to investigate the role of the quencher in the material, the same conditions (energy and velocity) were used for the fabrication of 500 nm period woodpile structures using a material that did not contain the 2-(dimethylamino)ethyl methacrylate monomer, which acts as a polymerization quencher. Figure 19, shows a SEM image of such a structure.

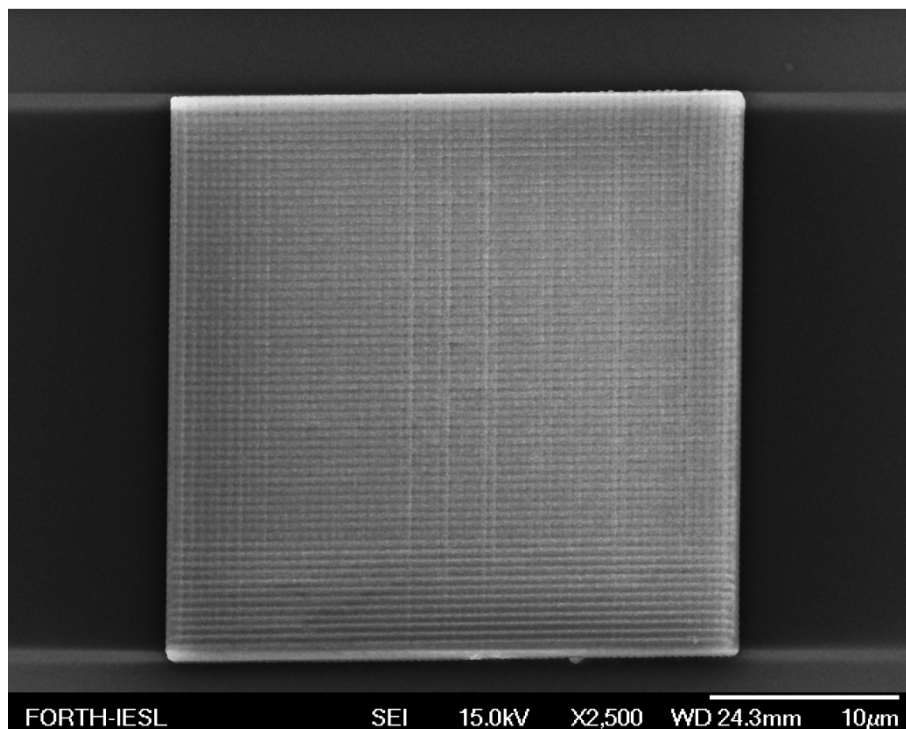


Figure 19. Woodpile structure with 500 nm rod spacing, fabricated using the same hybrid material without the chemical quencher.

As it is obvious, in this case the intralayer gaps are fully polymerized, and the woodpile in fact is a solid polymer block, allowing us to conclude that the role of the quencher is essential to obtain the increased resolution.

3.2.2 White light diffraction

In order to ensure the structural characteristics and the high quality periodicity of the photonic structures, diffraction experiments were carried out. The woodpile structures are periodically ordered media with a square symmetry in the planes in between the layers and thus, when an incoming light beam travels in the positive z axis direction (normal incidence), diffraction patterns should appear.

If the layers of the woodpile structure are parallel to the xy plane, then primitive lattice vectors \mathbf{a}_1 and \mathbf{a}_2 can be defined. Then the primitive reciprocal lattice vectors can be defined as \mathbf{b}_1 and \mathbf{b}_2 and any reciprocal lattice vector \mathbf{g} can be expressed as a combination of these two primitive reciprocal lattice vectors $\mathbf{g} = p\mathbf{b}_1 + q\mathbf{b}_2$, where p,q is a pair of integers. In normal incidence, the wavevector of a diffracted beam emerging from the structure can be written as $\mathbf{K}_g^\pm = \mathbf{g} \pm \sqrt{k^2 - |\mathbf{g}|^2} \hat{\mathbf{z}}$ where, the +(-) sign corresponds to a transmitted (reflected) beam, $k = 2\pi/\lambda$ is the magnitude of the incident wave vector and λ is the wavelength. Each refracted beam corresponds to a propagating wave if the z component of \mathbf{K}_g^\pm is purely real [45]. Then, diffraction channels will open when $|\mathbf{g}| < k$ and we have diffraction cutoff when ever $|\mathbf{g}| = k$. For square lattices this condition reduces to [44]

$$\frac{d}{\lambda} = \frac{1}{n} \sqrt{p^2 + q^2}$$

where, n is the refractive index of the diffraction medium, λ is the wavelength of the incident radiation and d is the periodicity of the layers in the perpendicular direction. In air (n=1) four diffraction channels will open, that correspond to:

$$(p,q) = (1,0), (0,1), (-1,0), (0,-1)$$

$$\text{when } \frac{d}{\lambda} \geq 1 \Rightarrow d \geq \lambda .$$

The second set of diffracted beams appears for

$$(p,q) = (1,1), (1,-1), (-1,1), (-1,-1)$$

when $d > \lambda$

According to the above, when a white light beam strikes the structure in normal incidence, the first four channels will be observed for all the fabricated structures, since the condition $d > \lambda$ holds. The difference will lay in the observed colors. From $d=900$ nm to $d=700$ nm the whole visible spectrum is diffracted since the period of the woodpile structure is larger than any visible wavelength of the white light beam (figures 20, 21).

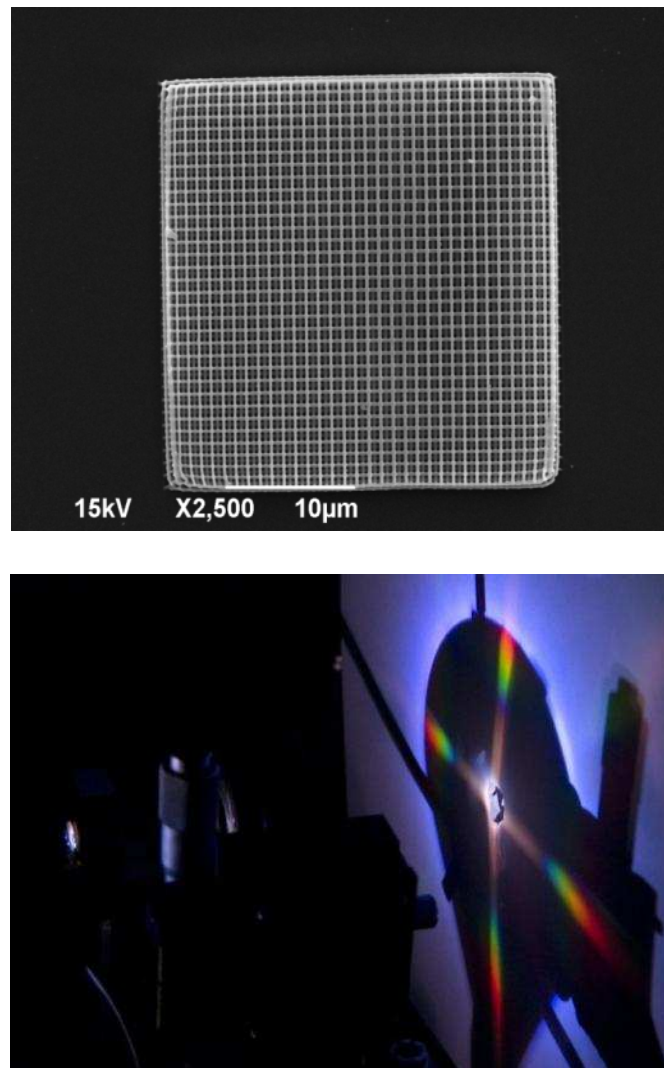


Figure 20. a) SEM image of a woodpile structure of 900 nm in rod periodicity b) white light diffraction pattern of the same structure. All visible wavelengths are observed.

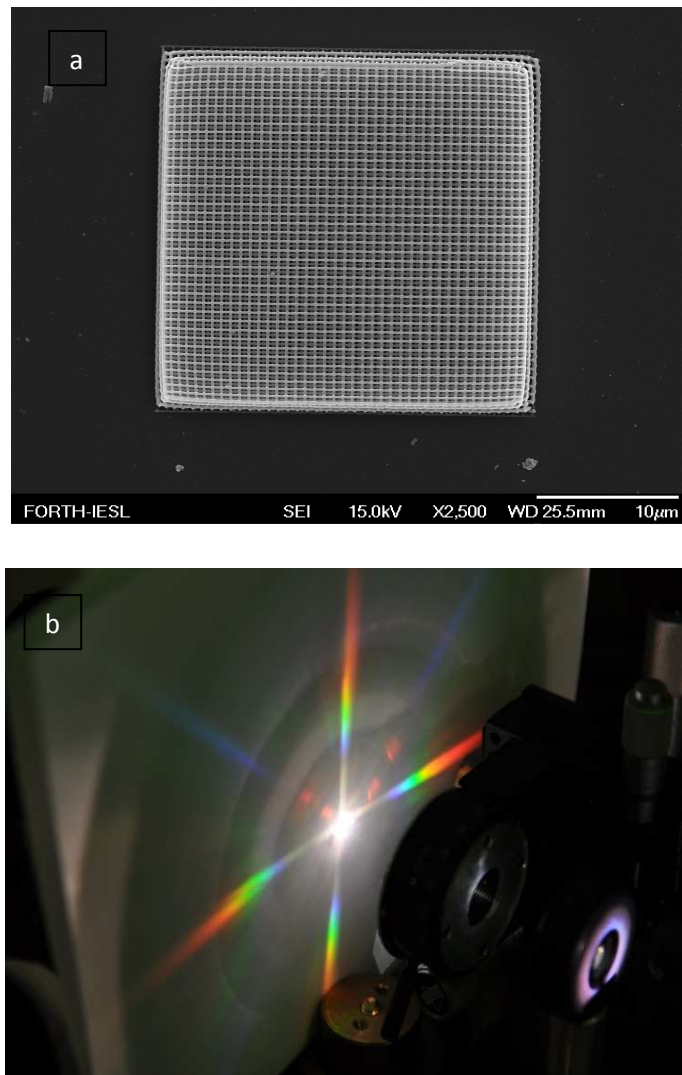


Figure 21. a) SEM image of a 700 nm period woodpile structure b) white light diffraction pattern of the same structure. Again all visible wavelengths are observed.

As the period of the structures moves down to wavelengths close to the visible spectrum such as $d = 600$ nm and $d = 500$ nm a cutoff in the diffracted beams is observed. At $d = 600$ nm a red cutoff exists (figure 22) while for the 500 nm period structures the green and red diffracted beams are no longer visible (figure 23).

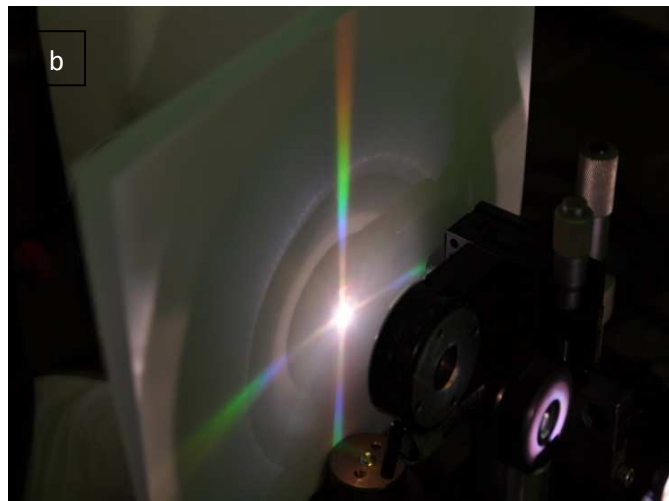
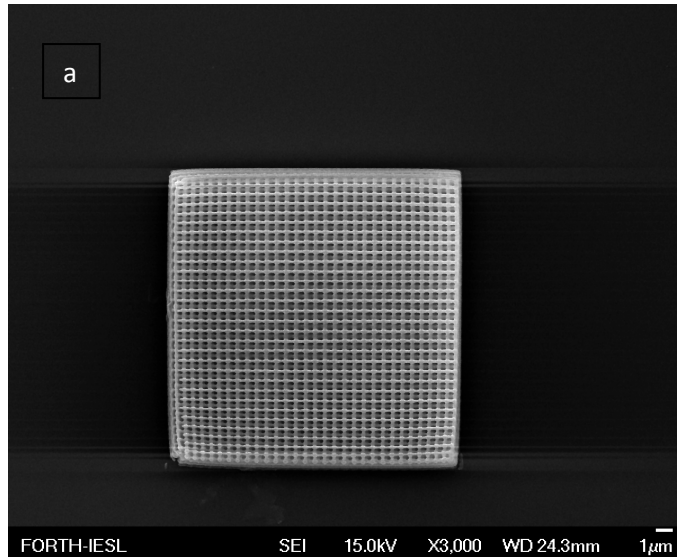
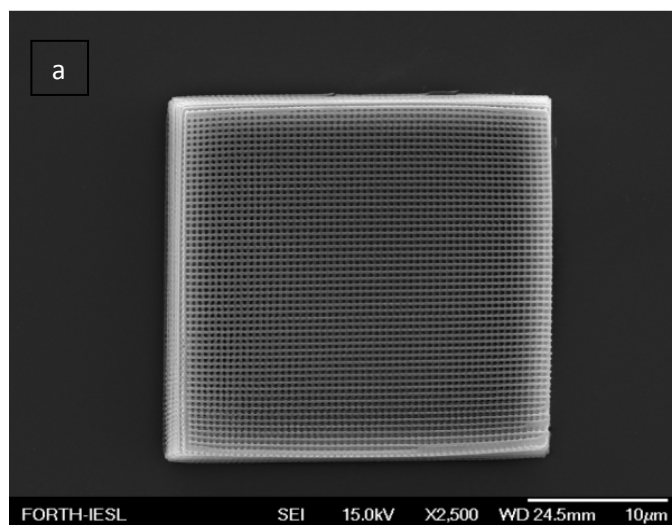


Figure 22.a) SEM image of a 600 nm period woodpile structure **b)** white light diffraction pattern of the same structure. A red cutoff is observed



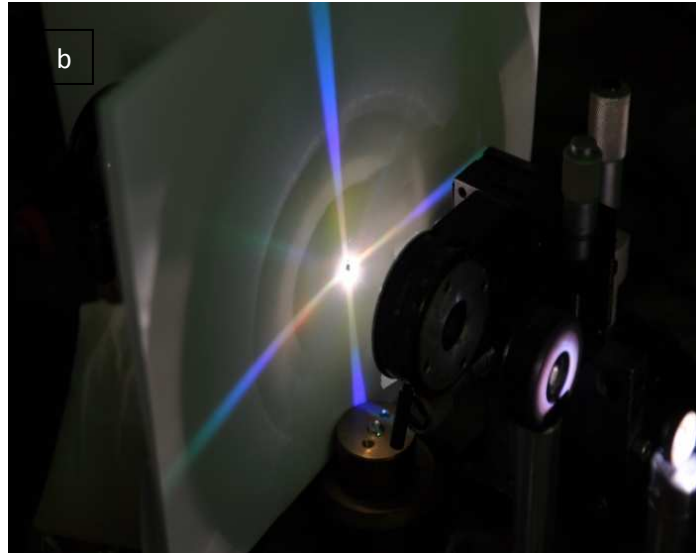
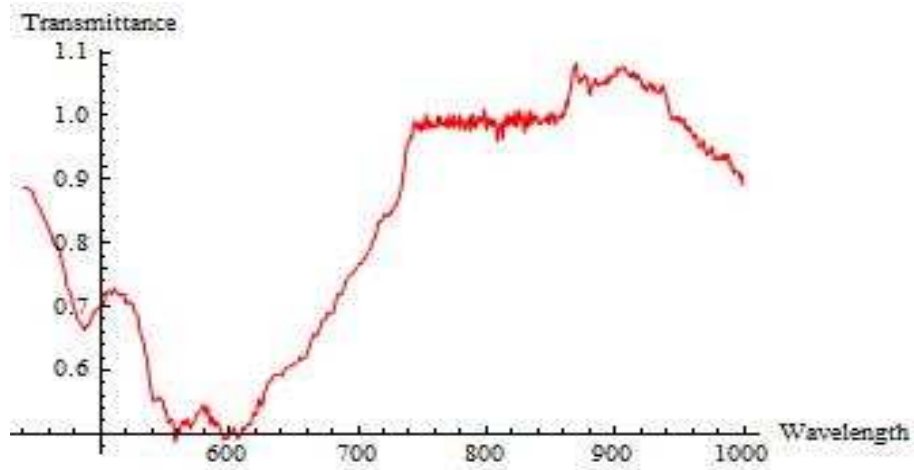


Figure 23. a) SEM image of a 500 nm period woodpile structure b) white light diffraction pattern of the same structure. A red and green cutoff is observed

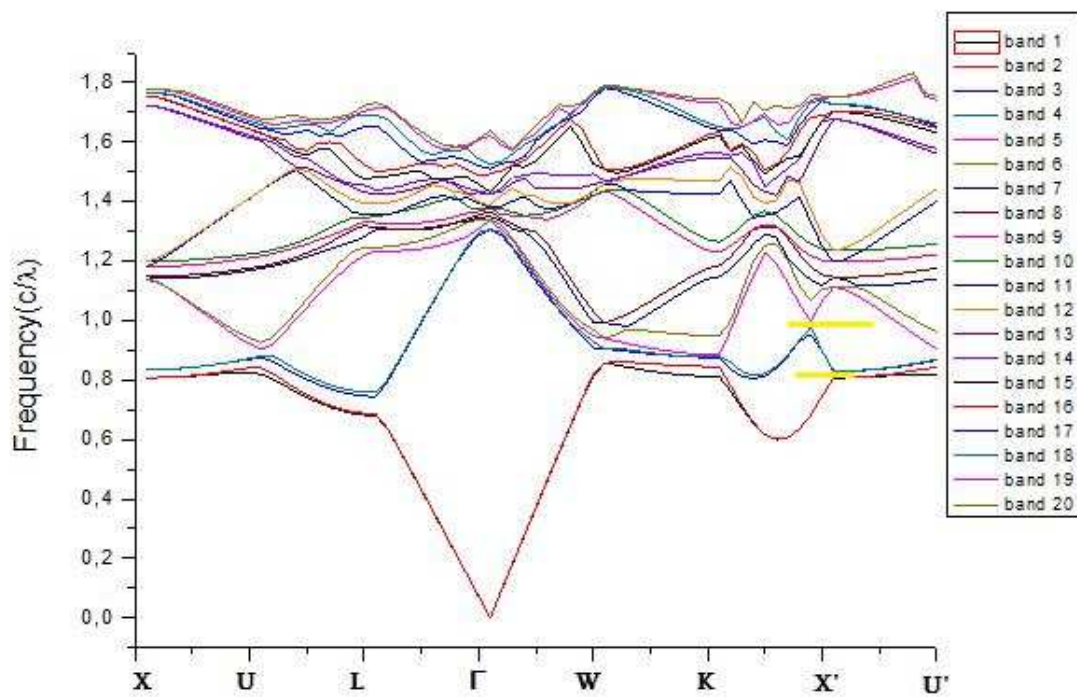
In addition to the four spots molding the cross, another set appears along the diagonal direction. Still, these channels are observed as on goes from $d = 900$ nm to $d = 700$ nm. In the case of $d = 900$ nm $\Rightarrow \lambda < 900$ nm / $\sqrt{2} = 636$ nm the red part is nearly diffracted, whereas for $d = 700$ nm $\Rightarrow \lambda < 700$ nm / $\sqrt{2} = 495$ nm the red part is cutoff and the green part is just diffracted. However, for $d = 600$ nm $\Rightarrow \lambda < 600$ nm / $\sqrt{2} = 424$ nm and $d = 500$ nm $\Rightarrow \lambda < 500$ nm / $\sqrt{2} = 353$ nm the visible wavelengths are limited, thus no diagonal spots are observed.

3.2.3 Pump probe

The pump probe experiment was carried out for the 500 nm period woodpile structures doped with CdS quantum dots. Pump on and pump off transmittance spectra were recorded. The optical response of the sample is shown in figures 24 and 25.



(a)



(b)

Figure 24. a) transmittance spectrum of the 500 nm woodpile structure with probe beam b) theoretical calculation for the bandgaps of 500 nm woodpile structure.

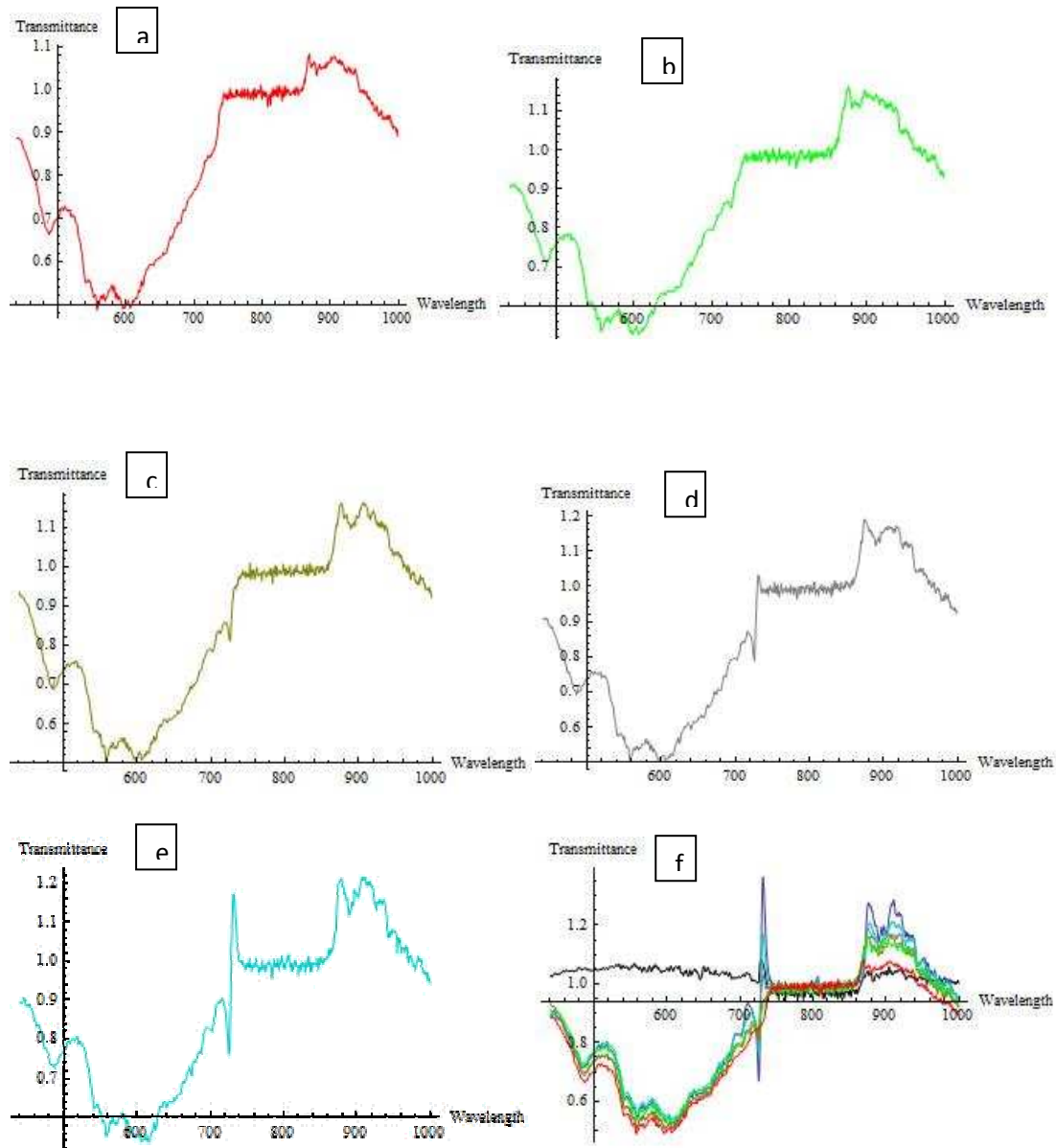


Figure 25. a) Probe beam optical response of the sample b-e) pump beam optical response at different time intervals f) summary plot of spectra a-e.

Figure 24(a) shows the transmittance spectrum of the woodpile structure as recorded with the probe beam. Two dips are observed around 730 nm and 870 nm that correspond to the 1st and 2nd order bandgaps of the structure. These are in agreement with the theoretical calculation (figure 24(b)). The laser wavelength is at 800 nm so appropriate filter was used in order to elide the area between 750 – 850 nm. Thus, this is a “blind area”.

In figure 25, the transmittance of the sample is recorded with the pump on. Spectra b-e show the optical response of the sample at different time intervals. Figure 25(f) shows a summary of plots a-e for better correlation. The black line corresponds to the

background noise recorded with the bare glass only. After the pump beam strikes the structure, there is an enhancement of the transmittance dips that were observed during the probe measurements. The high intensity pump beam induces a change in the refractive index due to the optical Kerr effect. This change is clearly observed at the recorded spectra. The dips are clearly sharper, deeper and wider in relation to the linear measurements. These first measurements do not clearly reveal a wavelength shift of the bandgaps that is expected for 3rd order nonlinear photonics crystals. Further experiments that include more accurate equipment used in the setup are being held for the observation of the shift and the completion of the pump probe experiment. In any case, the first results are very promising and open the way for the fabrication of 3rd order nonlinear photonic crystals.

3.3 Conclusions

We presented our investigations in the synthesis of novel hybrid photosensitive materials that can be accurately structured using direct laser writing. We succeeded in the fabrication of a hybrid material that contains cadmium methacrylate which serves as a precursor for the in situ synthesis of CdS quantum dots. A quencher molecule incorporated in the material gave us the ability to fabricate 3D photonic crystals, using the two-photon polymerization technique, with period down to 500 nm and resolution below 100 nm which is far beyond the diffraction limit. Diffraction patterns of the photonic crystals revealed their perfect periodicity. CdS quantum dots enrich the material with 3rd order nonlinearity which was observed from the characteristic peak valley graph using the Z-scan technique. The ability of the material to vary its refractive index under high intensity electromagnetic radiation and its use in the fabrication of 3D photonic crystals open the way for optical switching devices that are going to play an important role in future technology of telecommunications and optical computing.

References

- [1] C. J. Brinker and G. W. Scherrer, "Sol-Gel Science The physics and chemistry of sol-gel processing." Academic Press, 1990.
- [2] G. Kickelbick, "Introduction to Hybrid Materials," in *Hybrid Materials: Synthesis, Characterization, and Applications*, Wiley, 2007, pp. 1–47.
- [3] H. Schmidt, "Inorganic-organic composites by sol-gel techniques," *Journal of Sol-Gel Science and Technology*, vol. 1, no. 3, pp. 217–231, 1994.
- [4] a Doraiswamy, C. Jin, R. J. Narayan, P. Mageswaran, P. Mente, R. Modi, R. Auyeung, D. B. Chrisey, a Ovsianikov, and B. Chichkov, "Two photon induced polymerization of organic-inorganic hybrid biomaterials for microstructured medical devices.," *Acta biomaterialia*, vol. 2, no. 3, pp. 267–75, May 2006.
- [5] K.-S. Lee, D.-Y. Yang, S. H. Park, and R. H. Kim, "Recent developments in the use of two-photon polymerization in precise 2D and 3D microfabrications," *Polymers for Advanced Technologies*, vol. 17, no. 2, pp. 72–82, Feb. 2006.
- [6] B. N. Chichkov and A. Ostendorf, "Two-Photon Polymerization: A New Approach to Micromachining," *Photonics Spectra*, no. October, 2006.
- [7] H. Sun and S. Kawata, "Two-Photon Photopolymerization and 3D Lithographic Microfabrication," *Quantum*, pp. 169–274, 2004.
- [8] C. N. LaFratta, J. T. Fourkas, T. Baldacchini, and R. a Farrer, "Multiphoton fabrication.," *Angewandte Chemie (International ed. in English)*, vol. 46, no. 33, pp. 6238–58, Jan. 2007.
- [9] G. Filippidis, J. Catherine, M. Farsari, V. Zorba, and C. Fotakis, "Construction of micron three-dimensional structures employing multi-photon polymerization," *Proceedings of the Institution of Mechanical Engineers, Part N: Journal of Nanoengineering and Nanosystems*, vol. 219, no. 4, pp. 165–168, Jan. 2005.
- [10] J. Serbin, a Egbert, a Ostendorf, B. N. Chichkov, R. Houbertz, G. Domann, J. Schulz, C. Cronauer, L. Fröhlich, and M. Popall, "Femtosecond laser-induced two-photon polymerization of inorganic-organic hybrid materials for applications in photonics.," *Optics letters*, vol. 28, no. 5, pp. 301–3, Mar. 2003.
- [11] a. Ovsianikov, a. Gaidukeviciute, B. N. Chichkov, M. Oubaha, B. D. MacCraith, I. Sakellari, a. Giakoumaki, D. Gray, M. Vamvakaki, M. Farsari, and C. Fotakis, "Two-Photon Polymerization of Hybrid Sol-Gel Materials for Photonics Applications," *Laser Chemistry*, vol. 2008, pp. 1–7, 2008.
- [12] M. Malinauskas, A. Gaidukevičiūtė, V. Purlys, A. Žukauskas, I. Sakellari, E. Kabouraki, A. Candiani, D. Gray, S. Pissadakis, R. Gadonas, A. Piskarskas, C. Fotakis, M. Vamvakaki, and M. Farsari, "Direct laser writing of microoptical structures using a Ge-containing hybrid material," *Metamaterials*, vol. 5, no. 2–3, pp. 135–140, Jun. 2011.

- [13] a. Ovsianikov, a. Ostendorf, and B. N. Chichkov, "Three-dimensional photofabrication with femtosecond lasers for applications in photonics and biomedicine," *Applied Surface Science*, vol. 253, no. 15, pp. 6599–6602, May 2007.
- [14] A. Ovsianikov, S. Schlie, A. Ngezhahayo, A. Haverich, and B. N. Chichkov, "Two-photon polymerization technique for microfabrication of CAD-designed 3D scaffolds from commercially available photosensitive materials," *Journal of Tissue Engineering and Regenerative Medicine*, vol. 1, pp. 443–449, 2008.
- [15] V. Melissinaki, a a Gill, I. Ortega, M. Vamvakaki, a Ranella, J. W. Haycock, C. Fotakis, M. Farsari, and F. Claeysens, "Direct laser writing of 3D scaffolds for neural tissue engineering applications.," *Biofabrication*, vol. 3, no. 4, p. 045005, Dec. 2011.
- [16] R. Guo, Z. Li, Z. Jiang, D. Yuan, W. Huang, and A. Xia, "Log-pile photonic crystal fabricated by two-photon photopolymerization," *Journal of Optics A: Pure and Applied Optics*, vol. 7, no. 8, pp. 396–399, Aug. 2005.
- [17] S. Psycharakis, A. Tosca, V. Melissinaki, A. Giakoumaki, and A. Ranella, "Tailor-made three-dimensional hybrid scaffolds for cell cultures.," *Biomedical materials (Bristol, England)*, vol. 6, no. 4, p. 045008, Aug. 2011.
- [18] B. Jia, D. Buso, J. van Embden, J. Li, and M. Gu, "Highly non-linear quantum dot doped nanocomposites for functional three-dimensional structures generated by two-photon polymerization.," *Advanced materials (Deerfield Beach, Fla.)*, vol. 22, no. 22, pp. 2463–7, Jun. 2010.
- [19] X. Li, D. Steel, D. Gammon, and L. J. Sham, "on Optically Driven Semiconductor Quantum Dots," *Optics & Photonics News*, no. September, 2004.
- [20] M. Betcke and H. Voss, "Electronic states of quantum dots," pp. 1–20.
- [21] T. Kippeny, L. a. Swafford, and S. J. Rosenthal, "Semiconductor Nanocrystals: A Powerful Visual Aid for Introducing the Particle in a Box," *Journal of Chemical Education*, vol. 79, no. 9, p. 1094, Sep. 2002.
- [22] P. N. Prasad and D. J. Williams, "Introduction to Nonlinear Optical Effects in Molecules and Polymers," *Wiley*, 1991.
- [23] R. W. Boyd, *Nonlinear Optics*, Third Edit. Academic Press, 2008.
- [24] D. Wang, "Semiconductor nanocrystal-polymer composites: using polymers for nanocrystal processing," in *Semiconductor Nanocrystal Quantum Dots*, A. L. Rogach, Ed. Springer New York, 2008, pp. 171–196.
- [25] J. Li, B. Jia, G. Zhou, C. Bullen, J. Serbin, and M. Gu, "Spectral Redistribution in Spontaneous Emission from Quantum-Dot-Infiltrated 3D Woodpile Photonic Crystals for Telecommunications," *Advanced Materials*, vol. 19, no. 20, pp. 3276–3280, Sep. 2007.
- [26] P. Bhattacharya, J. Sabarinathan, J. Topol'ancik, and S. Chakravarty, "Quantum Dot Photonic Crystal Light Sources," *Proceedings of the IEEE*, vol. 93, no. 10, pp. 1825–1838, Oct. 2005.

- [27] R. H. Lipson and C. Lu, "Photonic crystals: a unique partnership between light and matter," *European Journal of Physics*, vol. 30, pp. 33–48, 2009.
- [28] E. Yablonovitch, "Photonic Crystals: What 's in a Name?," *Physical Review Letters*, no. March, pp. 12–13, 2007.
- [29] F. Koenderink, "Emission and Transport of Light in Photonic Crystals," Universiteit van Amsterdam, 2003.
- [30] J. D. Joannopoulos and S. G. Johnson, *Photonic Crystals: Molding the Flow of Light*. Princeton University Press, 2008.
- [31] a. Ovsianikov, a. Gaidukeviciute, B. N. Chichkov, M. Oubaha, B. D. MacCraith, I. Sakellari, a. Giakoumaki, D. Gray, M. Vamvakaki, M. Farsari, and C. Fotakis, "Two-Photon Polymerization of Hybrid Sol-Gel Materials for Photonics Applications," *Laser Chemistry*, vol. 2008, pp. 1–7, 2008.
- [32] Z.-B. Sun, X.-Z. Dong, S. Nakanishi, W.-Q. Chen, X.-M. Duan, and S. Kawata, "Log-pile photonic crystal of CdS–polymer nanocomposites fabricated by combination of two-photon polymerization and in situ synthesis," *Applied Physics A*, vol. 86, no. 4, pp. 427–431, Jan. 2007.
- [33] a Carrassi and S. Abati, "Introduction to scanning electron microscopy," *Mondo odontostomatologico*, vol. 29, no. 2, pp. 29–36.
- [34] "Scanning Electron Microscope." [Online]. Available: <http://www.purdue.edu/rem/rs/sem.htm>.
- [35] B. M. Weckhuysen, "Ultraviolet-Visible Spectroscopy," in *In Situ Spectroscopy of Catalysts*, American Scientific Publishers, 2004, pp. 255–270.
- [36] J. Ren, *Principles and Applications of Fluorescence Spectroscopy*. Blackwell Science, 2007.
- [37] R. Jenkins, "X-ray Techniques: Overview," *Encyclopedia of Analytical Chemistry*. Wiley, pp. 13269–13288, 2000.
- [38] A. Dement and A. Jovai, "Pulse Shape Influence on the Accuracy of Z-scan Measurements," *Nonlinear Analysis: Modeling and Control*, vol. 10, no. 2, pp. 119–136, 2005.
- [39] M. Sheik-Bahae, "sensitive measurement of optical nonlinearities using a single beam," *Journal of Quantum Electronics*, vol. 26, no. 4, pp. 760–769, 1990.
- [40] F. García-Santamaría, J. Galisteo-López, P. Braun, and C. López, "Optical diffraction and high-energy features in three-dimensional photonic crystals," *Physical Review B*, vol. 71, no. 19, pp. 1–5, May 2005.
- [41] T. G. Euser, P. J. Harding, and W. L. Vos, "Broadband sensitive pump-probe setup for ultrafast optical switching of photonic nanostructures and semiconductors.," *The Review of scientific instruments*, vol. 80, no. 7, p. 073104, Jul. 2009.

- [42] M. N. Kalasad, M. K. Rabinal, B. G. Mulimani, and G. S. Avadhani, "Temporal evolution of capped cadmium sulfide nanoparticles," *Semiconductor Science and Technology*, vol. 23, no. 4, p. 045009, Apr. 2008.
- [43] A. Ovsianikov and B. N. Chichkov, "Two-Photon Polymerization-High Resolution 3D Laser Technology and Its Applications," in *Nanoelectronics and Photonics*, A. Korkin and F. Rosei, Eds. New York, NY: Springer New York, 2008, pp. 427–446.
- [44] I. Sakellari, E. Kabouraki, D. Gray, V. Purlys, C. Fotakis, A. Pikulin, N. Bityurin, M. Vamvakaki, and M. Farsari, "Diffusion-Assisted High-Resolution Direct Femtosecond Laser Writing," *ACS Nano*, vol. 6, no. 3, pp. 2302–2311, 2012.
- [45] L. Dorado, R. Depine, D. Schinca, G. Lozano, and H. Míguez, "Experimental and theoretical analysis of the intensity of beams diffracted by three-dimensional photonic crystals," *Physical Review B*, vol. 78, no. 7, pp. 1–5, Aug. 2008.

